



# In situ X-ray computed micro-tomography imaging of failure processes in Cr-coated Zircaloy nuclear fuel cladding materials

Guanjie Yuan<sup>a</sup>, J. Paul Forna-Kreutzer<sup>a</sup>, Jon Ell<sup>b</sup>, Harold Barnard<sup>c</sup>, Benjamin R. Maier<sup>d</sup>, Edward Lahoda<sup>d</sup>, Jorie Walters<sup>e</sup>, Robert O. Ritchie<sup>b</sup>, Dong Liu<sup>a,\*</sup>

<sup>a</sup> School of Physics, University of Bristol, Bristol, UK

<sup>b</sup> Department of Materials Science and Engineering, University of California, Berkeley, USA

<sup>c</sup> Advanced Light Source, Lawrence Berkeley National Laboratory, Berkeley, USA

<sup>d</sup> Westinghouse Electric Company LLC, Churchill, PA, USA

<sup>e</sup> Westinghouse Electric Company LLC, Columbia, SC, USA

## ARTICLE INFO

### Keywords:

Coated-Zircaloy fuel cladding  
C-ring compression  
X-ray computed micro-tomography  
Deformation and fracture

## ABSTRACT

Chromium (Cr)-coated Zircaloy fuel cladding has been considered a promising candidate materials system for accident tolerant fuels. In this work, two types of Cr coatings produced by cold sprayed (CS) and physical vapour deposited (PVD) methods were studied. In particular, a novel combination of C-ring compression tests at room temperature (RT) and 345 °C in an inert gas environment and real-time X-ray micro-computed tomography (XCT) imaging was adopted to investigate the failure processes. Before testing, the crystal structure and local properties were fully characterized; post testing, *ex situ* scanning electron microscope (SEM) imaging were conducted to complement the XCT measurements in crack density. It was found that the failure processes in both coatings vary with temperature, as discussed in detail. The hoop strength of first coating cracks' formation of CS materials were higher than the PVD materials due to their higher interfacial roughness and distribution of splatted grains in CS coating. Based on a calculation of the first Dundurs' parameter from the measured local properties and observed crack arrest/deflection at coating/substrate interface, it was found that the cold sprayed coating-cladding material system has a higher interfacial toughness in terms of critical strain energy release rate due to its interlocking interfacial structure.

## 1. Introduction

Due to its low neutron absorption, good corrosion resistance and excellent mechanical properties, Zirconium-based alloys (Zircaloy) have been utilized as fuel cladding materials in light water nuclear reactors (LWRs) for decades [1,2]. However, during design-basis accident (DBA) and loss of-coolant accident (LOCA) conditions, Zircaloy can rapidly oxidize in high-temperature steam and release combustible hydrogen gas, which could lead to serious incidents like the 2011 Fukushima accident [3,4]. As a consequence, the concept of accident tolerant fuels (ATFs) has been raised in order to improve the safety performance of nuclear fuels under, and beyond, DBA and LOCA conditions, as well as improving their performance under normal operating conditions, e.g., at ~ 345 °C [3,5–7].

Two main solutions have been considered by ATF designs: the long-term plan is to replace the Zircaloy by other materials, e.g., iron-

chromium-aluminium (FeCrAl) alloys or SiC fibre-reinforced SiC matrix composites (SiC<sub>f</sub>-SiC<sub>m</sub>) [6,8]; the near-term solution is to add an oxidation-resistance coating on the outer surface of current Zircaloy cladding tubes [3]. Among various coating materials, Cr is widely chosen due to its extraordinary corrosion and oxidation resistance, high melting point, high strength, as well as its chemical compatibility with Zircaloy [7,9,10]. Indeed, many research studies have been carried out on the Cr-coated Zircaloy alloys and showed promising results [3,4,6,7,9].

There are two common methods for applying Cr coatings onto the Zircaloy substrate, namely cold spraying (CS) and physical vapour deposition (PVD). For the CS process, the Cr particles are accelerated to a very high speed by the carrier gas, which is forced through a spray nozzle; upon impact, the Cr particles deform plastically and bond mechanically to the substrate to form a coating [6,11], and splatted Cr grains and gaps/porosity between grains are commonly formed in the

\* Corresponding author.

E-mail address: [Dong.Liu@bristol.ac.uk](mailto:Dong.Liu@bristol.ac.uk) (D. Liu).

<https://doi.org/10.1016/j.matdes.2023.112373>

Received 23 May 2023; Received in revised form 24 September 2023; Accepted 26 September 2023

Available online 27 September 2023

0264-1275/© 2023 The Authors. Published by Elsevier Ltd. This is an open access article under the CC BY license (<http://creativecommons.org/licenses/by/4.0/>).

coating. In comparison, for PVD method, Cr materials are firstly vapourised and then deposited onto the substrate surface to form the coating [12], formed columnar Cr grains in the coating. These two coating processes result in varied crystallite sizes and structures which subsequently affect the coating crack behaviours [3]: for CS Cr-coated materials under loading, coating cracks commonly propagated along the boundaries of the splatted grains and formed tortuous crack pathways, as been reported by Roache *et al.* [13] (2022) from their plug-expansion tests at RT and Burden *et al.* [14] (2023) from their C-ring compression tests at RT; as for PVD Cr-coated materials under loading at RT (e.g., tensile tests [15] and C-ring compression tests [14]), coating cracks tended to travelled along the boundaries of the columnar Cr grains and cleavage crack behaviours were commonly reported. Additionally, for CS Cr-coated materials, the manufacturing process of CS coating caused plastic deformation of both Cr coating and underlying substrate at the coating/substrate interface area [6,11], which may result in the variation of local properties of coating and substrate at the interface area, and could subsequently affect the mechanical performance of the entire cladding system. However, the openly-published literatures mostly focus on the local properties and mechanical integrity of the CS and PVD Cr coating [3,6,7,9], only few reported the local properties and microstructures of the underlying substrate at the interface area [11]. Therefore, to get a comprehensive understanding of the mechanical properties of Cr-coated Zircaloy cladding, it is necessary to investigate the influence of coating process to the underlying substrate (e.g., variation of local properties measuring by nanoindentation method), which provides insights into the structural integrity of the overall Cr-coated cladding material system. In this work, the CS and PVD Cr-coated Zircaloy cladding tube materials were investigated in terms of their deformation and fracture behaviour at room temperature (RT) and at 345 °C, and the local properties of coating and substrate at the interface area of these two types of materials were thoroughly analysed by nanoindentation method.

In terms of prior studies, Umretiya *et al.* [3] (2020) conducted ring compression tests at room temperature on their PVD and CS Cr-coated Zircaloy-4 cladding tube materials (outer diameter of 9.5 mm and wall-thickness of 0.51 mm), with a coating thickness of  $6.48 \pm 1.41 \mu\text{m}$  and  $29.00 \pm 2.00 \mu\text{m}$ , respectively; they found the peak load and yield strength of the CS coated materials (398.36 N and 6.13 MPa) to be slightly higher than that of the PVD coated materials (371.36 N and 5.79 MPa), which they attributed to the thicker Cr coating of CS materials. Roache *et al.* [13] (2022) performed *in situ* plug-expansion tests at 315 °C on CS Cr-coated Zircaloy cladding materials (coating thickness:  $\sim 24 \mu\text{m}$ ) using digital image correlation (DIC) and acoustic emissions (AE) methods. The hoop strains were reported to be  $\sim 0.34\%$  for crack initiation in the coating, with a hoop strength of  $\sim 500$  MPa. To better understand the fracture process under loading, studies have recently combined mechanical testing with real-time 2D scanning electron microscope (SEM) imaging. For example, Nguyen *et al.* [15] (2022) conducted *in situ* uniaxial tensile tests in the SEM on PVD Cr-coated (coating thickness:  $\sim 15 \mu\text{m}$ ) sheet Zircaloy samples ( $60 \times 14 \times 1.2 \text{ mm}^3$ ) at RT. They found that cracks were directly observed to have initiated from the edges of sample, with the density of cracks increasing with applying load to reach a maximum (saturated) level of 9–10 cracks per mm (i.e., distance between coating cracks is  $\sim 100$  to  $110 \mu\text{m}$ ) at a maximum tensile stress ( $\sim 400$  MPa). Jiang *et al.* [16] (2021) also performed *in situ* tensile tests on their PVD Cr-coated (coating thickness:  $\sim 15 \mu\text{m}$ ) Zircaloy sheet specimens ( $20 \times 3 \times 0.6 \text{ mm}^3$ ) at elevated temperatures (from RT to 500 °C). This study found a  $\sim 60\%$  reduction in tensile strength with increasing temperature - specifically  $\sim 430$  MPa at RT and  $\sim 160$  MPa at 500 °C - and a reduction in the saturated crack densities with increasing temperature observed by real-time SEM imaging - specifically  $\sim 15$  cracks per mm (i.e., distance between cracks is  $\sim 66 \mu\text{m}$ ) at RT and  $\sim 3$  cracks per mm (i.e., distance between cracks is  $\sim 330 \mu\text{m}$ ) at 450 °C. However, despite these pertinent studies, the 2D SEM images could only offer 2D microstructural information of the coating cracks on either the

coating surface or the cross-sections at the sample's edge, and there is still a lack of 3D image characterization to capture the failure processes, together with microstructural information, for the evolution of damage in such materials in real-time under load at relevant elevated temperatures, and eventually improving the design of such coated Zircaloy cladding materials for further industrial application. To achieve this, X-ray computed micro-tomography (XCT) is a promising non-destructive 3D imaging method which has been used in Zircaloy materials; it has also been used to quantify the internal porosities in welded joints [17]. By combining the XCT method with *in-situ* mechanical testing, direct 3D characterisation of the damage evolution in such coated cladding system can be acquired. Such experiments have been successfully utilized in capturing microstructural evolution in nuclear graphite,  $\text{SiC}_f\text{-SiC}_m$  cladding materials, oxide-oxide ceramic-matrix composites and alumina-alumina ceramic-matrix composites at elevated temperatures above 1000 °C [18–21]. Among various loading configurations (e.g., plug-expansion, ring-compression), the C-ring compression setup is a reliable method for measuring hoop strength, simulating crack formation and propagation processes in Zircaloy cladding tube materials [14,22,23], provides relevant and convenient mechanical integrity assessment of such nuclear fuel cladding tube materials [23]. Additionally, C-ring compression configuration is more representative (compare with tensile tests) of the service conditions of such cladding materials, as they were internal pressured under industrial application.

In this study, a unique device was utilized for *in situ* synchrotron X-ray micro-tomography imaging of crack initiation and propagation in Cr-coated Zircaloy cladding materials under C-ring compression at temperatures up to 345 °C. The microstructures and local properties of as-received materials were thoroughly characterized by respectively nanoindentation and electron backscatter diffraction (EBSD) prior to the high temperature testing. Subsequent characterisation using scanning electron microscopy (SEM) were carried out to assist the understanding of fracture processes. As far as the authors are aware, there have been no openly published high-temperature mechanical experiments combined with real-time X-ray computed micro-tomography imaging in these materials which highlights the novelty of the current work.

## 2. Experimental procedures

### 2.1. Materials and sample preparation

Two types of Zircaloy cladding tube materials were investigated, including a cold sprayed Cr-coated Zircaloy (CS) and a physical vapour deposited Cr-coated Zircaloy (PVD); they were provided by Westinghouse Electric Company LLC; detailed fabrication processes can be found in refs [3,6]. A schematic illustration of the configuration of C-ring compression test setup is presented in Fig. 1.

The outer radius ( $r_o$ ), inner radius ( $r_i$ ) and wall-thickness ( $t$ ) of these two types of Zircaloy cladding tube materials were estimated from the X-ray computed micro-tomography images; the values are listed in Table 1. The outer radius  $r_o$  is in the range of 4.58 to 4.59 mm, with  $r_i = 3.94$  mm and the wall thickness  $t = 0.64\text{--}0.65$  mm. The  $r_i/r_o$  ratios of these two types of cladding materials are all approximately 0.86. For X-ray tomography tests, samples were prepared using a CUTLAM®1.1 manual cutting machine combined with a water-based coolant. A slow speed diamond saw (operating at 230 rpm) was used to cut C-ring samples (with a width in the range of 2 to 3 mm) from the cladding tubes. Prior to the beamline experiment, all C-ring samples were air-dried for more than 24 hrs.

For nanoindentation and EBSD mapping, the CS and PVD Cr-coated materials were first mounted by a BUEHLER SimpliMet™ XPS1 hot compression mounting machine at a pressure of 3 MPa and temperature of 180 °C with 180 s of both heating and cooling times. Samples were then ground with 400-grit ( $\sim 2$  mins), 600-grit ( $\sim 2$  mins), 800-grit ( $\sim 4$  mins), 1200-grit ( $\sim 5$  mins), 2500-grit ( $\sim 5$  mins) and 4000-grit ( $\sim 5$  mins) sand grinding disks, with each step grinded off the scratches from

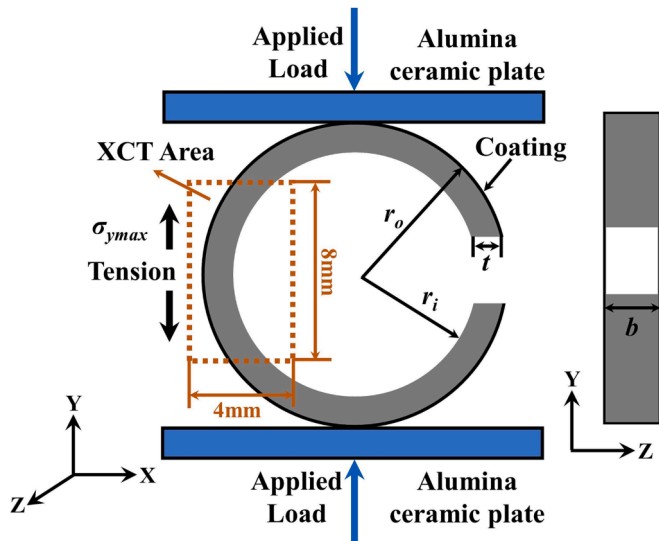


**Fig. 1.** Schematic of the C-ring compression test setup including the coordinate system and a typical sample geometry.  $r_o$  is the outer radius,  $r_i$  is the inner radius,  $t$  is the wall-thickness and  $b$  is the width of the C-ring sample. The *in-situ* synchrotron X-ray tomography scans (as marked by dashed rectangular) were collected at the maximum hoop stress/strain region of the tested C-ring sample.

**Table 1**  
Dimensions of Zircaloy cladding tube specimens.

	$r_o$ (mm)	$r_i$ (mm)	$t$ (mm)
CS	$4.59 \pm 0.014$	$3.94 \pm 0.052$	$0.65 \pm 0.035$
PVD	$4.58 \pm 0.018$	$3.94 \pm 0.076$	$0.64 \pm 0.034$

the previous step [24]. Then, samples were polished with 3  $\mu\text{m}$  (MD-Nap cloth) in 1  $\mu\text{m}$  water-based diamond suspensions ( $\sim 4$  mins at 260 rpm for each polishing step). After that, samples were further polished by a BUEHLER vibratory polisher for  $\sim 12$  hrs with colloidal silica suspension, to achieve a flat surface with minimal surface deformation [25]. Finally, the surface of the samples was cleaned in water and ethanol and air-dried for more than three days prior to testing.

## 2.2. Nanoindentation testing

Nanoindentation measurements were conducted on the polished cross-sections of the as-received CS and PVD Cr-coated cladding materials using a Hysitron TI Premier nanoindenter with a Berkovich diamond tip. To correct before the measurement's possible geometrical deviations from an ideal Berkovich shape, a tip area function was generated by a calibration process on fused silica. A thin layer of crystalbond adhesive was then used to mount polished sample cross-sections on the loading stage, with a  $50\times$  objective lens to verify the locations of each indent. During the indentation process, a depth control was used with  $100 \text{ nm s}^{-1}$  for both loading and unloading rates with holding at a depth of 500 nm for 2 s. All indents were placed more than 5  $\mu\text{m}$  apart from each other. The hardness ( $H$ ) and elastic modulus ( $E$ ) were calculated using the Oliver and Pharr method [26], from Eqs. (1) and (2), respectively:

$$H = \frac{P_{Max}}{A_r} \quad (1)$$

$$\frac{1}{E_r} = \frac{1 - \nu_i^2}{E_i} + \frac{1 - \nu_s^2}{E} \quad (2)$$

where  $P_{Max}$  is the maximum applied load (mN),  $A_r$  is the projected contact area,  $E_i$  and  $\nu_i$  are the elastic modulus and Poisson's ratio of the

tip (1140 GPa and 0.07), respectively.  $E_r$  is the reduced modulus of the tested sample. A Poisson's ratio  $\nu_s$  of 0.21 [7] and 0.30 [27] was used for Cr coatings and Zircaloy substrate, respectively.

## 2.3. Scanning electron microscopy imaging

Scanning electron microscopy (SEM) images of the post-tested C-ring specimens were performed using a Hitachi S3500N variable pressure scanning electron microscope operating at a current of 62  $\mu\text{A}$ , with a 20 kV accelerating voltage.

## 2.4. Electron backscatter diffraction mapping

Electron backscatter diffraction (EBSD) maps of the polished cross-sections of the CS and PVD Cr coatings were acquired using a TESCAN Mira3 XMH variable pressure scanning electron microscope with an Oxford Instrument Nordlys EBSD detector at the United Kingdom Atomic Energy Authority (UKAEA); an accelerating voltage of 20 kV was used with each specimen tilted to an angle of  $70^\circ$ . Oxford Instruments® HKL™ Channel 5™ software was used to acquire and analyse the colour orientation imaging microscopy maps, band contrast graphs and inverse pole figures (IPFs) for both the CS and PVD Cr coatings.

## 2.5. In situ C-ring compression with X-ray computed micro-tomography

*In situ* high temperature C-ring compression tests combined with synchrotron X-ray computed micro-tomography (XCT) imaging were conducted on the CS and PVD Cr-coated cladding tube materials, on beamline 8.3.2 at the Advanced Light Source (Lawrence Berkeley National Laboratory, U.S.). During the tests, an unique high-temperature testing device was used; further details of which can be found in refs [21,28–30]. The C-ring sample's geometry is shown in Fig. 1. When a compressive load was applied, the maximum hoop stress ( $\sigma_{ymax}$ ) was calculated following ASTM Standard C1323-16 [22] from the relationship:

$$\sigma_{ymax} = \frac{P_U R}{b t r_o} \left[ \frac{r_o - r_a}{r_a - R} \right], \quad (4)$$

where  $P_U$  is the maximum applied load (peak load),  $b$  is the width of specimen. The average radius  $r_a$  and the term  $R$  are respectively defined by Eqs. (5) and (6).

$$r_a = \left( \frac{r_o + r_i}{2} \right) \quad (5)$$

$$R = \frac{r_o - r_i}{\ln \frac{r_o}{r_i}} \quad (6)$$

Note that according to ASTM C1323-16, to minimize the circumferential stress variation across the sample width [22], the width of the C-ring sample should not surpass twice of its wall-thickness. However, such constraint has been relaxed by Embree *et al.* [31] from their finite element analysis (FEA) on various  $b/t$  ratio combinations, as tabulated in Table S1 in the Supplementary Materials. In the current study, the  $b/t$  ratios of the C-ring samples were between  $\sim 3.4$  and  $\sim 3.9$ . Based on ref. [31], the calculated hoop stress was at least an order of magnitude higher than the axial stress on the sample's outmost surface, which is sufficient for the sample to fracture by hoop tension in the X-ray tomography imaged areas. Additionally, based on FEA calculation conducted by Embree *et al.* [31], the values of hoop stresses were found similar on the sample's outmost surface with radian of the C-ring samples of around  $\pm 45^\circ$  against the middle plane, as presented in Fig. S1 in the Supplementary Materials.

During the C-ring compression tests, each sample was loaded monotonically to the peak load ( $P_U$ ) in an Ar atmosphere at room temperature and  $345^\circ\text{C}$ . A thermocouple was attached to the sample surface to calibrate the temperature; the *in-situ* loading experiment was

conducted after the temperature stabilised at  $345 \pm 2$  °C. A small pre-load ( $\sim 5$ N) was applied to all the samples to avoid sample movement during the scanning process. A real-time radiography projection was used to monitor the position of sample, as well as monitor the formation of cracks. Displacement controlled loading at a speed of  $\sim 0.5$   $\mu\text{m/s}$  was used to ensure quasi-static loading. Four to six XCT scans were collected at increasing loading steps for each sample. A list of the XCT scans at the loading steps normalised to the peak load are presented in Table S2 in the Supplementary Materials. At each temperature, two specimens were tested.

During each XCT scan, a 6 to 43 keV white light X-ray beam was used with a PCO Edge 2  $\times$  CCD detector, 2560  $\times$  2560 pixels, and a pixel size of  $3.25 \times 3.25$   $\mu\text{m}$ . The field of view of the X-ray tomography imaging was 8  $\times$  4 mm focused on the C-ring sample's middle section with the highest deformation stresses, marked in Fig. 1 by the dashed line. For each scan, 1969 projections were collected over a 180° rotation with a 30 ms acquisition time for each projection (around 5 mins for each XCT scan). Noted that, the selected XCT resolution (3.25  $\mu\text{m}/\text{pixel}$ ) is to compromise for the testing time of each sample; if the resolution was increased (e.g., 0.65  $\mu\text{m}/\text{pixel}$ ), the scanning period for each scan will be increased from  $\sim 5$  mins to more than 35 mins, which significantly increases the experimental time for each sample ( $\sim 6$  hrs for each sample) and limited the tested number of samples. XCT reconstruction was performed with a Gridrec algorithm [32] in the TomoPy package [33]. The centre of rotation of each scan was automatically detected and then individually manually identified to account for deformation artefacts. To reduce the fixed-pattern noise of the detector and improve the spatial resolution of each scan, a conventional flat field correction was used. All reconstructed scans were converted to stacks of 32-bit tiff images and were imported to open-source software ImageJ [34] to convert them to 8-bit raw data files. These raw data files were imported into Avizo Lite software (version 2020.1) [35] for visualization of the coating cracks. To be noted that, to reduce the influence of the variation of tensile stress along the C-ring sample's hoop direction to the coating crack behaviours, all reconstructed XCT images were cropped into selected range, with the radian of the C-ring samples of around  $\pm 13^\circ$  against the samples' middle plane (based on FEA calculation by Embree *et al.* [31], see Fig. S1), and only coating cracks in the selected range were selected to analysis their formation and progressive propagation.

### 3. Results

#### 3.1. Microstructure

Typical microstructures of polished cross-sections of the as-received CS and PVD Cr-coated materials are shown in Fig. 2a and Fig. 2b, respectively. The CS Cr coating/substrate interface is tortuous, with some small pores scattered in the coating, as marked by the black arrows in Fig. 2a. For the PVD Cr coating, the coating/substrate interface is

relatively flat, with no obvious defects in the form of cracks or porosity found in the coating, at the resolution shown in Fig. 2b. The thickness of the CS and PVD Cr coatings were measured to be  $20.03 \pm 3.93$   $\mu\text{m}$  and  $14.36 \pm 0.16$   $\mu\text{m}$ , respectively.

The band contrast graphs and corresponding orientation image microscopy maps of the CS and PVD coatings are presented in Fig. 3a and Fig. 3b, respectively. The CS Cr coating has the typical splat structure with small, closed gaps or pores in between (Fig. 3a). The orientation image microscopy map shows that the CS Cr grains have a random orientation in each splat (Fig. 3a); there is no obvious preferred Cr grain orientation in the CS coating as evident in the IPF map (Fig. 3c). For the PVD Cr coating, the Cr grains are primarily columnar in shape, with smaller grains found clustered near the coating/substrate interface (Fig. 3b). Compared with the CS coating, no obvious porosity/gaps between grains are found (Fig. 3b), consistent with Fig. 2. The PVD Cr grains show strong texture, in the X and Y directions; most of them are along [1 1 1] direction (Fig. 3d). Measurements of the areas of the Cr grains in the CS and PVD coatings indicate that the Cr grains in the CS coating are in the range of 0.01 to 7.25  $\mu\text{m}^2$ , whereas the grains in the PVD coating are in the range of 0.01 to 16.35  $\mu\text{m}^2$ . The area distribution of the Cr grains (selected range of 0 to 1  $\mu\text{m}^2$  where most grains distribute) in the CS and PVD Cr coatings are presented in Fig. 3c and Fig. 3d, respectively. For both types of Cr coatings, more than 50% of the Cr grains are in the range of 0 to 0.1  $\mu\text{m}^2$ . The average area of the Cr grains in the CS coating is  $0.16 \pm 0.42$   $\mu\text{m}^2$ , while the PVD Cr grains have a higher ( $\sim 140\%$ ) average area of  $0.39 \pm 1.22$   $\mu\text{m}^2$ .

#### 3.2. Local mechanical properties

Nanoindentation tests were conducted on polished cross-sections of both the CS and PVD Cr-coated cladding materials in four areas: (i) in the middle of the Cr coating (termed as 'Area #1'), (ii) in the Cr coating but located 3  $\mu\text{m}$  or less to the coating/substrate interface ('Area #2'), (iii) in the substrate but located within 5  $\mu\text{m}$  of the interface ('Area #3'), and (iv) in an area in the substrate away from the interface, i.e., an area where properties are potentially not impacted by the coating process ('Area #4'). Examples of the four indent areas are shown in Fig. 4; the data points are tabulated in Table 2.

For the CS Cr-coated material, Area #1 had an average hardness ( $H$ ) of  $4.49 \pm 0.65$  GPa and an elastic modulus ( $E$ ) of  $266.06 \pm 7.96$  GPa; Area #2 displayed lower values of both hardness and modulus (compared with Area #1), which were  $3.79 \pm 0.34$  GPa and  $249.47 \pm 8.85$  GPa, respectively. The substrate region had an overall lower hardness and elastic modulus than the coating; specifically, Area #3 had a hardness of  $3.02 \pm 0.18$  GPa and elastic modulus of  $109.53 \pm 5.25$  GPa, and Area #4 had a hardness of  $2.62 \pm 0.13$  GPa and modulus of  $105.61 \pm 4.99$  GPa. It is evident that in the substrate, the region close to the interface (Area #3) has a higher hardness ( $\sim 15.3\%$ ) compared to the region away from the interface (Area #4), which implies that the cold

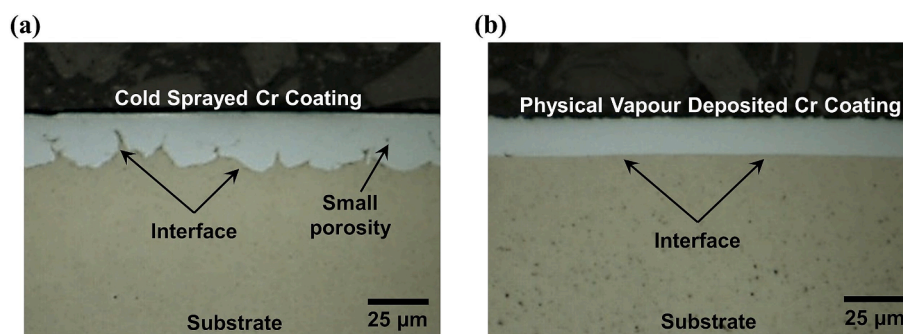
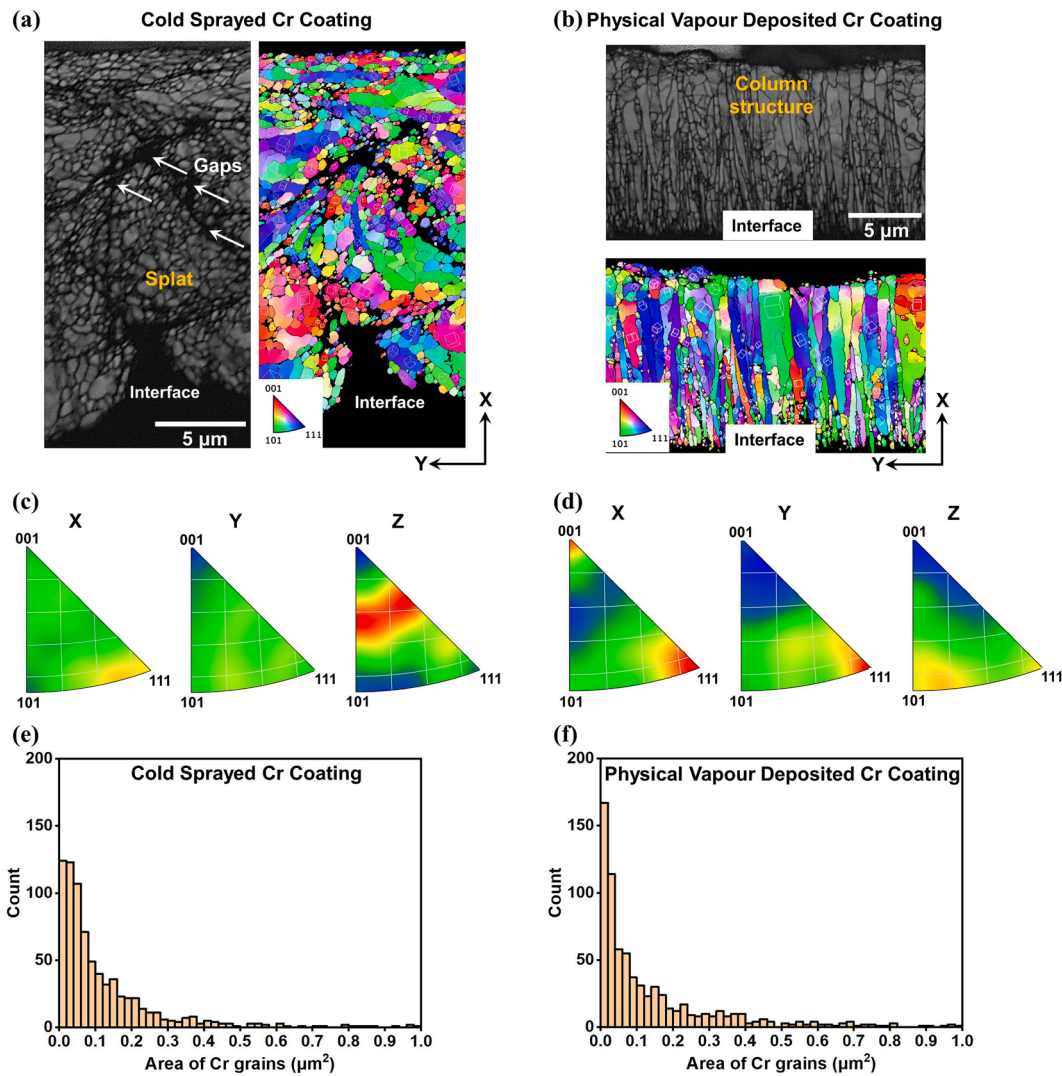


Fig. 2. Optical images of the polished cross-sections of the as-received Cr-coated Zircaloy cladding tube materials: (a) cold sprayed (CS) Cr-coated materials showing a tortuous coating/matrix interface and small pores distributed in the coating (marked by black arrows), and (b) physical vapour deposited (PVD) Cr-coated materials with Cr coating showing a flat interface.



**Fig. 3.** (a) and (b) are EBSD maps of the Cr coatings showing band contrast graphs; the colour orientation imaging microscopy maps show the Cr grains of X-Y plane. (a) the cold sprayed (CS) Cr coating shows splat structures and small gaps/pores (marked by white arrows) between splats which are consistent to the small pores observed in Fig. 2; (b) the physical vapour deposited (PVD) Cr coating shows columnar structured Cr grains with no obvious porosity; (c) and (d) are inverse pole figures (IPFs) show textures of the Cr grains in the coatings: (c) shows random orientation of Cr grains in the CS Cr coating, and (d) shows the Cr grains in the PVD Cr coating; Cr grains are mostly along the [1 1 1] direction in the X and Y directions; (e) and (f) are measured area distribution graphs of Cr grains in the coatings (in the range of 0 to 1 μm<sup>2</sup>) for the (e) CS Cr coating, and (f) PVD Cr coating.

spraying process has hardened the surface layer of the substrate.

For the PVD Cr-coated material, an average hardness ( $H$ ) of  $4.47 \pm 0.35$  GPa and an elastic modulus ( $E$ ) of  $268.31 \pm 6.92$  GPa were measured for Area #1. In comparison, Area 2 had similar elastic modulus ( $260.03 \pm 4.88$  GPa) but a  $\sim 16.3\%$  higher hardness value -  $5.20 \pm 0.45$  GPa, the latter being expected due to the smaller grain size at the interface (based on the EBSD results). For the substrate, the overall hardness and elastic modulus values were lower compared to the coating; no significant differences in either value were found for Area #3 ( $2.72 \pm 0.25$  GPa and  $113.41 \pm 5.26$  GPa) and Area #4 ( $2.64 \pm 0.23$  GPa and  $109.52 \pm 3.97$  GPa). This demonstrates that the PVD coating process did not cause obvious changes in the substrate close to the coating interface.

### 3.3. Hoop strength at room temperature and 345 °C

As little change was found in the mechanical behaviour of two (repeat) samples of either the CS or PVD materials tested at each temperature, one representative load–displacement curve for the CS and PVD Cr-coated cladding material tested at each condition (RT and

345 °C) are plotted in Fig. 5.

The maximum hoop strength derived from Eq. (4) are listed in Table 3. Note that as the sample deformation in the current test was larger than the validity criteria cited in ASTM Standard C1323-16 [22], the calculated values may be taken as overestimates. For both types of cladding materials, the maximum hoop strengths at RT are higher than that at 345 °C. Specifically, the maximum hoop strength for CS Cr-coated materials are  $\sim 1141$ – $1194$  MPa at RT,  $\sim 77\%$  higher than that at 345 °C ( $\sim 603$ – $695$  MPa). The same trend is found for PVD materials where the maximum hoop strengths are  $\sim 1150$  MPa at RT,  $\sim 88\%$  higher than that at 345 °C ( $\sim 591$ – $631$  MPa). Additionally, as described in Section 2.5, real-time radiography projections were used to monitor coating cracks during loading; the loads and corresponding hoop stresses (derived from Eq. (4)) when these cracks were first observed by radiography projection (also confirmed with XCT images) are listed in Table 3. For CS Cr-coated materials tested at both RT and 345 °C, coating cracks were first seen at  $\sim 90\%$  of the peak load, with corresponding measured stresses of  $\sim 1020$  MPa and  $\sim 584$  MPa, respectively. As for PVD Cr-coated materials tested at both RT and 345 °C, coating cracks were detected at  $\sim 80\%$  of the peak load ( $P_U$ ),

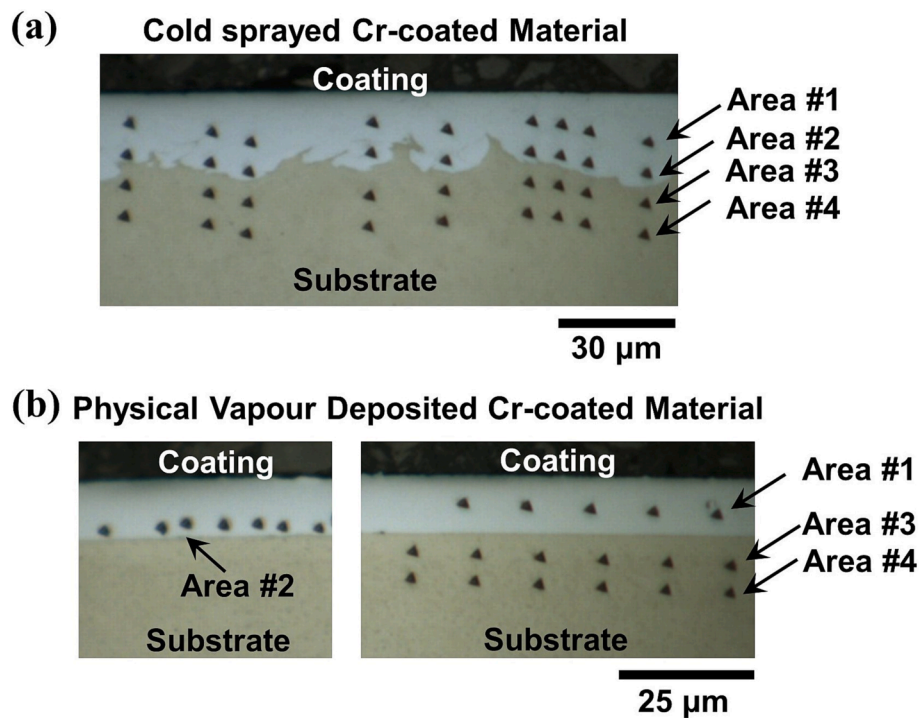


**Fig. 4.** Optical images of the polished cross-sections of the as-received Cr-coated Zircaloy cladding tube materials showing the four areas of the indents, including in the middle of the Cr coating (termed 'Area #1'), in the Cr coating but located at 3  $\mu\text{m}$  or less from the coating/substrate interface ('Area #2'), in the substrate but located within 5  $\mu\text{m}$  of the interface ('Area #3'), and in the substrate away from the interface ('Area #4'), for the (a) cold sprayed (CS) and (b) physical vapour deposited Cr (PVD) coated materials.

**Table 2**

Measured values of the hardness  $H$  and elastic modulus  $E$  in different areas of the polished cross-sections of the cold sprayed (CS) and physical vapour deposited (PVD) Cr-coated Zircaloy cladding tube materials.

Areas	CS		PVD	
	$H(\text{GPa})$	$E(\text{GPa})$	$H(\text{GPa})$	$E(\text{GPa})$
Coating Area #1	$4.49 \pm 0.65$	$266.06 \pm 7.96$	$4.47 \pm 0.35$	$268.31 \pm 6.92$
	$3.79 \pm 0.34$	$249.47 \pm 8.85$	$5.20 \pm 0.45$	$260.03 \pm 4.88$
Coating Area #2	$3.02 \pm 0.18$	$109.53 \pm 5.25$	$2.72 \pm 0.25$	$113.41 \pm 5.26$
	$2.62 \pm 0.13$	$105.61 \pm 4.99$	$2.64 \pm 0.23$	$109.52 \pm 3.97$
Substrate Area #3				
Substrate Area #4				

with corresponding hoop stresses measured as  $\sim 897$  MPa and  $\sim 510$  MPa, respectively.

In current study, in addition to load drops (sudden decreasing of load at a fixed displacement), load relaxations (progressive decreasing of load at a fixed displacement, marked by coloured arrows in Fig. 5) were found for both types of cladding materials tested at both temperatures during the XCT scanning periods ( $\sim 5$  mins) when samples were held at constant displacement. Such load relaxations were also reported by Nguyen *et al.* [15] on room temperature tensile tests on PVD Cr-coated (coating thickness:  $\sim 15$   $\mu\text{m}$ ) sheet Zircaloy samples (example presented in Fig. S2 in the Supplementary Materials). The load relaxation values in current work may have some relationship with the mechanical properties of underlying Zircaloy substrate. While the in-depth analysis of these load relaxations was beyond the scope of current work, and detailed data of load relaxation values as a function of applied load are summarized in Table S3 in the Supplementary Materials.

### 3.4. Failure processes at room temperature and 345 °C

The failure processes of both types of cladding materials were investigated by analysing the real-time XCT scans collected at different loading steps. After went through more than 10,000 XCT slices, representative 2D XCT slices, as well as the 3D reconstructed images (shown in Fig. 6, Fig. 8, Fig. 10 and Fig. 12), are selected to illustrate the progressive failure processes of the coating cracks at both RT and 345 °C. Note these slices were extracted from the same location in the sample at increasing loading steps. After failure, the samples were further examined by SEM imaging. One representative sample from each coating type at each temperature was presented to provide a description of the failure process.

#### 3.4.1. Cold sprayed Cr-coated Zircaloy cladding material

For the cold sprayed sample S1 (tested at RT), the first XCT scan was collected at 31.36 N ( $0.64 P_U$ ; estimated hoop stress 723.23 MPa). However, no obvious cracks in the coating were visible in the real-time radiography projection, as well as the XCT scan with a pixel size of  $3.25 \times 3.25$   $\mu\text{m}$  (Fig. 6a). With continued loading, no cracks were seen in the radiography projection until 44.52 N ( $0.91 P_U$ ; estimated hoop stress 1091.17 MPa) where a XCT scan was collected. Multiple coating cracks were found to have formed simultaneously, Fig. 6b. Carefully investigation showed these cracks had similar behaviours; therefore, three of them (Crack#1 to #3, as marked in the magnified image in Fig. 6b) were selected as representative examples, and 3D visualization of part of these three representative cracks (selected range in a length of  $\sim 360$   $\mu\text{m}$ , which is  $\sim 15\%$  of the sample's total width:  $\sim 2.4$  mm) were presented in Fig. 6c. Once formed, all the coating cracks arrested at the coating/substrate interface without penetrating the underlying substrate (with examples presented in Fig. 6c); the majority of coating cracks travelled across the sample's total width ( $\sim 2.4$  mm) once formed, and some cracks were found stopped in the coating without travelling across the sample's total width, see Crack#3 in Fig. 6c. All the coating cracks

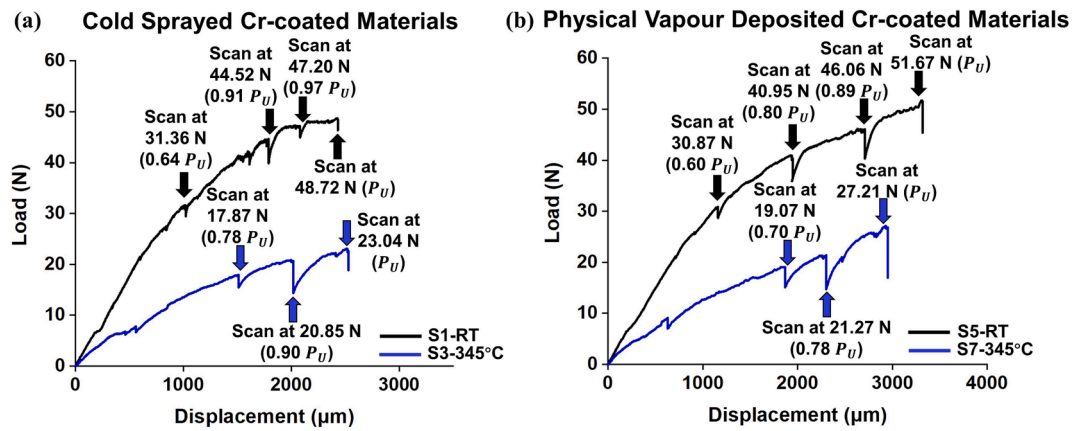


Fig. 5. Representative load–displacement curves for the C-ring compression tests of two types of Cr-coated Zircaloy cladding tubes at both room temperature and 345 °C: (a) cold sprayed (CS) Cr-coated materials including sample S1 tested at RT and sample S3 tested at 345 °C; (b) physical vapour deposited (PVD) Cr coated materials including sample S5 tested at RT and sample S7 tested at 345 °C. The coloured arrows indicate locations of the XCT scans and the associated load relaxations for the tested C-ring samples.

Table 3

The width of specimens, loads and corresponding hoop stresses where coating cracks were first observed, peak loads and calculated maximum hoop stresses for cold sprayed (CS) Cr-coated and physical vapour deposited (PVD) Cr-coated cladding materials tested at both RT and 345 °C.

Specimen	Sample width (mm)	Load and corresponding hoop stress where coating cracks were firstly observed	Peak load (N)	Maximum hoop stress (MPa)
CS-S1-RT	2.36 ± 0.10	44.52 N/1091.17 MPa	48.72	1194.11
CS-S2-RT	2.15 ± 0.10	35.27 N/948.90 MPa	42.42	1141.26
CS-S3-345 °C	2.21 ± 0.10	20.85 N/542.73 MPa	23.04	603.03
CS-S4-345 °C	2.40 ± 0.10	25.95 N/625.57 MPa	28.84	695.08
PVD-S5-RT	2.51 ± 0.10	40.95 N/921.33 MPa	51.67	1151.66
PVD-S6-RT	2.47 ± 0.10	38.66 N/873.26 MPa	50.73	1149.02
PVD-S7-345 °C	2.41 ± 0.10	21.27 N/492.68 MPa	27.21	631.64
PVD-S8-345 °C	2.18 ± 0.10	18.66 N/527.94 MPa	23.04	591.27

formed nearly perpendicular to the tensile hoop direction (Y direction), Fig. 6c. with toughening mechanisms (e.g., bifurcation (Crack#1) and un-cracked bridging (Crack#3) in Fig. 6c) being observed. The average distance between the coating cracks at this loading step was measured to be  $98.89 \pm 34.71 \mu\text{m}$ . Noted that the average distance between the coating cracks was measured by about 100 cross-sectional 2D XCT slices (X-Y plane) collected across the width of the tested samples, the value was also measured from the 3D segmentation and reconstruction of these coating cracks, and results showed good consistency. The same process applied to cold sprayed sample S2 (tested at RT) where the simultaneous formation of multiple cracks first occurred at  $0.89 P_U$  (35.27 N; 948.90 MPa). With increasing load to 47.20 N ( $0.97 P_U$ ; 1158.29 MPa) before the peak load ( $P_U$ ), the number of cracks increased, and a new crack (Crack#4) was observed in the selected range, Fig. 6d. Accordingly, the average distance between coating cracks reduced to  $77.60 \pm 25.41 \mu\text{m}$  (Fig. 6c). At peak load (48.72 N; 1194.11 MPa), the number of coating cracks further increased with a new crack (Crack#5) showed up in magnified image in Fig. 6e. The coating cracks were found still arrested at the coating/substrate interface (Fig. 6f). The newly formed cracks also travelled across the sample's total width (Crack#4 and #5 in Fig. 6f), with the further extended in length of the cracks

(across the sample' total width) formed in previous loading stages being observed (Crack#3 in Fig. 6f). The distance between the coating cracks was measured to reduce further to  $58.38 \pm 17.21 \mu\text{m}$  (Fig. 6f).

SEM images of the crack patterns of the CS sample S1 tested at RT are shown in Fig. 7. The image of the X-Y plane (Fig. 7a) shows that the cracks did not penetrate through to the substrate, which is consistent with the observations from XCT imaging (Fig. 6). These cracks formed nearly perpendicular (at an angle of  $80^\circ$  to  $95^\circ$ ) to the tensile hoop direction in the coating surface across the C-ring sample width (Fig. 7b), of the Y-Z plane), again consistent with the findings from the XCT images (Fig. 6). High magnification SEM images in Fig. 7c-e revealed various crack toughening mechanisms, including the creation of parallel cracks (Fig. 7c), uncracked ligament bridging (Fig. 7d) and cracks bifurcation (Fig. 7d and 7e). Crack deflection at the crack tips was also found, which can be as much as  $\sim 90^\circ$  to the crack length, typically along the strips on the coating formed during the CS manufacturing process (Fig. 7c). Crack bifurcation was observed to be either at the uncracked bridging areas (Fig. 7d) or along the crack (Fig. 7e). The width of these coating cracks was in the range of 1–5  $\mu\text{m}$ . The same observations were also observed in the CS sample S2 tested at RT.

For the CS Cr-coated sample S3 tested at 345 °C, the first XCT scan collected at 17.87 N ( $0.78 P_U$ ; 470.36 MPa) showed no obvious crack formation. With continued loading, no cracks were observed in the radiography projection until 20.85 N ( $0.90 P_U$ ; 542.73 MPa) where one XCT scan was collected (Fig. 8b). Distinct from the CS materials tested at RT, only three cracks showed up simultaneously (Fig. 8b); these three cracks were found showing similar behaviours, and Crack#1 (magnified image in Fig. 8b) was selected as representative example. 3D visualization of Crack#1 showed, once formed, it confined within the coating without penetrating the underlying substrate (Fig. 8c), and travelled across the sample's total width:  $\sim 2.2 \text{ mm}$  (21% of the total crack length was presented in Fig. 8c). Additionally, in some parts of Crack#1, crack deflection and bifurcation at the coating/substrate interface area was observed, Fig. 8b and 8c. The average distance between the coating cracks was measured to be  $334.67 \pm 154.31 \mu\text{m}$ ; which is much larger than that of the materials tested at RT ( $98.89 \pm 34.71 \mu\text{m}$ ) where coating cracks were first observed at 44.52 N ( $0.91 P_U$ ; 1091.17 MPa). These observations are consistent with CS sample S4 (tested at 345 °C) where three cracks were formed simultaneously at  $0.90 P_U$  (25.95 N; 625.57 MPa). With further loading to peak load (23.04 N; 695.08 MPa), the number of coating cracks did not increase with no markable changes found for the average distance between the coating cracks of  $314.89 \pm 141.77 \mu\text{m}$  (Fig. 8d). Coating cracks still arrested at the coating/substrate interface (Fig. 8e); with crack merging being observed (Fig. 8e) at the bifurcation and deflection area (same area in Fig. 8c) at the coating/

### Room Temperature Failure Process of Cold Sprayed Cr-coated Materials

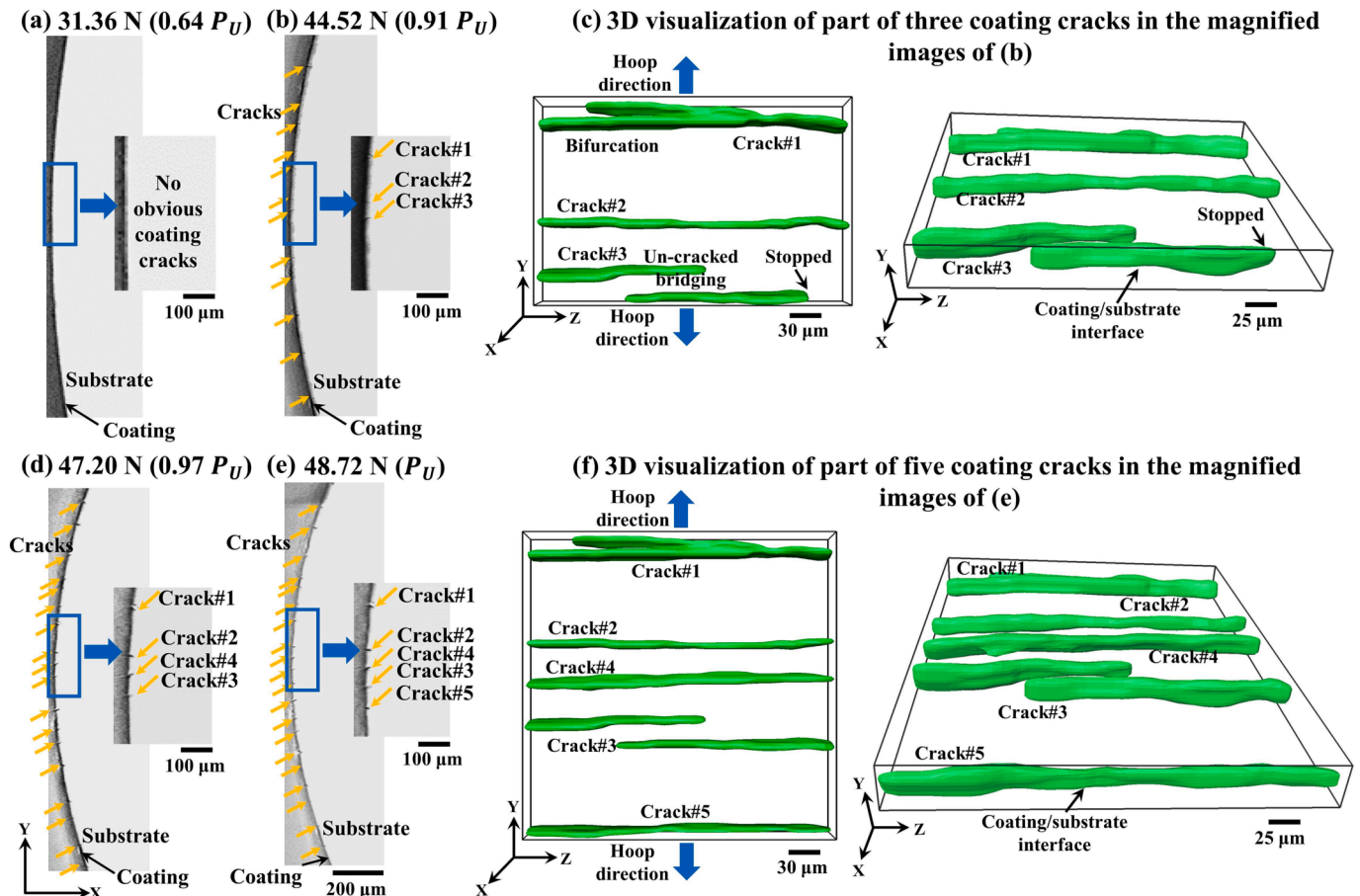


Fig. 6. (a), (b), (d) and (e) are *in situ* XCT slices of the X-Y plane (including magnified images extracted from the same location in the sample at increasing loading steps) showing crack formation and propagation processes in the cold sprayed (CS) Cr-coated materials tested at RT, as illustrated from sample S1: (a) scan at 31.36 N ( $0.64 P_U$ ) before peak load with no obvious coating cracks, (b) scan at 44.52 N ( $0.91 P_U$ ) before peak load where simultaneous coating cracks were firstly formed and captured by XCT imaging, (d) XCT scan at 47.20 N ( $0.97 P_U$ ) before peak load, and (e) XCT scan at peak load 48.72 N ( $P_U$ ). (c) and (f) are 3D visualization of part of the representative coating cracks (selected range in a length of  $\sim 360 \mu\text{m}$ , which is  $\sim 15\%$  of the total sample's width:  $\sim 2.4 \text{ mm}$ ) in the magnified images of (b) and (e) respectively. (c) shows Crack#1 to Crack#3 at 44.52 N ( $0.91 P_U$ ) before peak load; with Crack#1 and Crack#2 travelled through the total width of the sample, while Crack#3 stopped in the coating without travelling across the sample's total width. (f) shows Crack#1 to Crack#5 at peak load 48.72 N ( $P_U$ ); with Crack#4 and Crack#5 appeared with further load increase, and Crack#3 extended further in length and travelled across the sample's total width.

substrate interface.

SEM images of the crack patterns of the CS sample S3 tested at  $345^\circ\text{C}$  are shown in Fig. 9. Similar to the CS materials tested at RT, the cracks at  $345^\circ\text{C}$  arrested within the coating (consistent with XCT images in Fig. 8); crack deflection in the coating was also observed (Fig. 9a). From the surface of the Cr coating, primary coating cracks (with a width of  $\sim 6 \mu\text{m}$ ) formed perpendicular to the tensile hoop direction, as shown by the example in Fig. 9b. This is consistent with XCT imaging in Fig. 8. However, cracks with a finer width (less than  $3 \mu\text{m}$ , which is below the detection resolution of XCT and the radiography projection) were also observed as discontinuous and tortuous (Fig. 9b). SEM images indicated that deflection (Fig. 9d) and bifurcation (Fig. 9e) were observed at the tips of finer cracks. Similar observations were also found in CS sample S4 tested at the same temperature.

To summarize, for cold sprayed Cr-coated materials tested at both RT and  $345^\circ\text{C}$ , the first onset of multiple cracks was found at  $\sim 90\%$  peak load in the coating, these cracks reached coating/substrate interface and did not propagate into the substrate after reaching peak load. At RT, once formed, the majority of coating cracks tended to travel across the sample's total width; cracks formed almost perpendicular to the hoop direction. With further loading, number of cracks increased, and semi-across width cracks formed at previous loading stages further grew up

in length. However, at  $345^\circ\text{C}$ , only three primary cracks formed perpendicular to the hoop direction, accompanied by finer tortuous cracks. No coating spallation was found at either temperature.

#### 3.4.2. Physical vapour deposited Cr-coated Zircaloy cladding material

For the physical vapour deposited Cr coating sample S5 (tested at RT), the first XCT scan was collected at 30.87 N ( $0.60 P_U$ ; 715.93 MPa) with no obvious coating cracks observed (Fig. 10a). With further loading to 44.95 N ( $0.80 P_U$ ; 954.58 MPa), multiple cracks were first observed to have formed simultaneously. Similar behaviours were observed for these coating cracks, four of them (Crack#1 to Crack#4, as marked in the magnified image in Fig. 10b) were selected as representative examples, and part of these four representative cracks (selected length of  $\sim 540 \mu\text{m}$ , which is  $\sim 22\%$  of the sample's total width:  $\sim 2.5 \text{ mm}$ ) was visualized in 3D to illustrate the crack behaviours, Fig. 10c. All the cracks arrested at the coating/substrate interface once formed, see examples in Fig. 10c. The majority of coating cracks travelled across the sample's total width, with some of them did not travel across and arrested in the coating (Crack#1 and Crack#3 in Fig. 10c). Noted that, no direct correlation between the formation of Crack#3 and the sample boundary was found, which is direct evidence that not all the coating cracks generated from sample's edge. Some toughening mechanisms

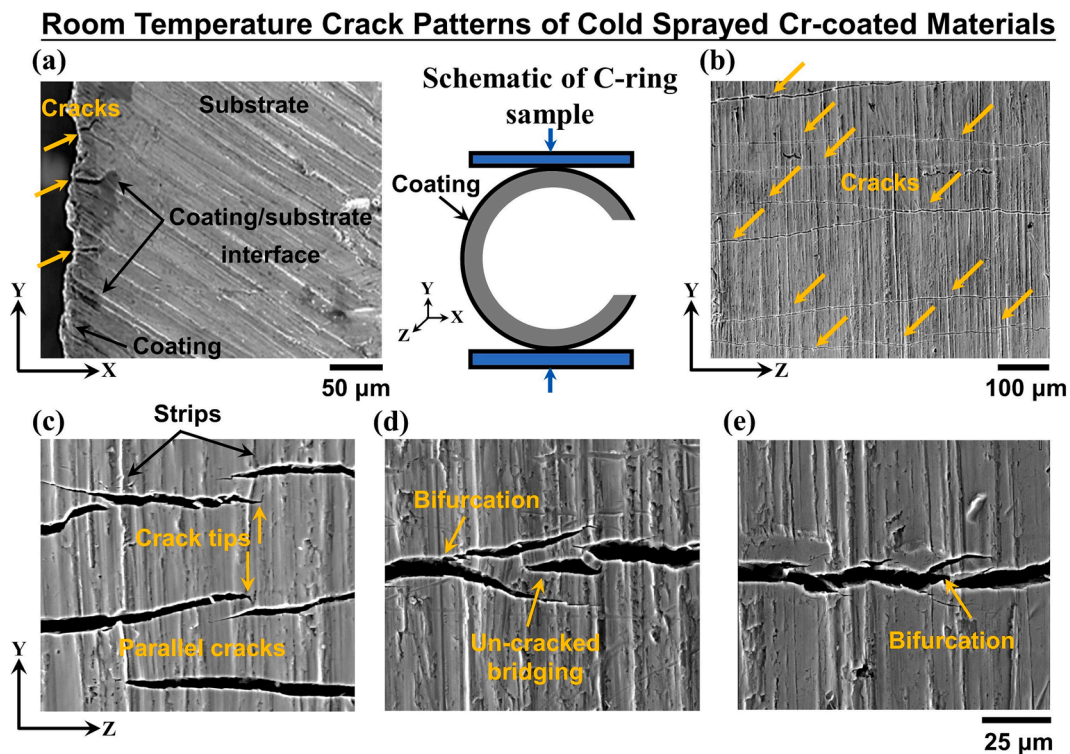


**Fig. 7.** SEM images showing crack patterns of post-failure cold sprayed (CS) Cr coated materials tested at room temperature, illustrated using sample S1: (a) image collected from the side surface of the sample (of the X-Y plane) showing multiple coating cracks, which did not penetrate through to the underlying substrate; (b) low magnification view of the outer surface of the sample (of the Y-Z plane) showing multiple cracks formed almost perpendicular (in the angle range of  $80^\circ$  to  $95^\circ$ ) to the tensile hoop direction of the sample; (c) to (e) are high magnification views of the outer surface of the sample (of the Y-Z plane): (c) shows parallel cracks and crack deflection at the crack tip up to  $\sim 90^\circ$  to the crack length (along the strips on the coating); (d) shows crack bifurcation at the uncracked ligament bridging areas, and (e) shows crack bifurcation along the crack length. One schematic of C-ring sample with loading is included.

were also observed, including un-cracked ligament bridging and deflection, see Crack#2 in Fig. 10c. The average distance between the coating cracks at this load was measured to be  $62.13 \pm 14.55 \mu\text{m}$ . In PVD sample S6 tested at RT, the first batch of cracks formed at a similar load:  $0.76 P_U$  (38.66 N; 952.59 MPa). With further loading to 46.06 N ( $0.89 P_U$ ; 1061.97 MPa), the distance between coating cracks reduced to  $50.67 \pm 14.92 \mu\text{m}$  (Fig. 10c). At peak load (51.67 N; 1193.22 MPa), the number of coating cracks further increased with Crack#5 newly formed, Fig. 10e. 3D visualization showed these five representative cracks arrested at the coating/composite interface, Fig. 10f; and the increasing of load led to Crack#1 and Crack#3 extended further in length with un-cracked ligament bridging. Additionally, at peak load, a new crack branched out from Crack#4, Fig. 10f. The distance between coating cracks further reduced to  $29.27 \pm 11.84 \mu\text{m}$  (Fig. 10d).

SEM imaging, conducted on the PVD materials tested at RT and shown by the cross-sectional view of sample S5 in Fig. 11a, has demonstrated the deflection of coating cracks at the coating/substrate interface. On the coating surface (of the Y-Z plane), these cracks are discontinuous in places and not all strictly perpendicular to the tensile hoop stress direction, specifically at an angle range of  $80^\circ$  to  $105^\circ$  (the maximum angle between coating cracks is  $\sim 25^\circ$ ) with the hoop direction (Fig. 11b). Magnified SEM images revealed that these cracks were mostly intergranular, Fig. 11. Several toughening mechanisms that include parallel cracks (Fig. 11c), cracks bifurcation (Fig. 11d) and un-cracked ligament bridging (Fig. 11e) were observed, shows consistency with the observation from XCT imaging. The width of coating cracks was in the range of 1–4  $\mu\text{m}$ . Similar observations were found for the PVD sample S6 tested at RT.

For the physical vapour deposited Cr coating sample S7 tested at  $345^\circ\text{C}$ , the first XCT scan was collected at 19.07 N ( $0.70 P_U$ ; 442.15 MPa) before peak load with no obvious coating cracks (Fig. 12a). With

further loading to 21.27 N ( $0.78 P_U$ ; 492.68 MPa), the XCT images collected at this load showed multiple coating cracks forming simultaneously (Fig. 12b). All these cracks arrested at the coating/substrate interface; with majority of them travelled through the total width of the C-ring sample ( $\sim 2.4 \text{ mm}$ ); representative cracks (Crack#1 to Crack#3) are shown in Fig. 12c. The average distance between the coating cracks was measured to be  $71.20 \pm 21.87 \mu\text{m}$ . In the PVD sample S8 tested at  $345^\circ\text{C}$ , the simultaneous formation of multiple cracks first occurred at a similar load of  $0.81 P_U$  (18.66 N; 527.94 MPa). At peak load (27.21 N; 660.72 MPa), the number of coating cracks increased (Fig. 12d) with Crack#4 and Crack#5 being observed in the magnified XCT images, Fig. 12d; and the 3D visualization of part of Crack#1 to Crack#5 is presented in Fig. 12e. Note that, as mark in Fig. 12e, the newly formed Crack#6 did not travel across the sample's total width, and was not observed in the selected XCT slice (X-Y plane) in Fig. 12d. At peak load, all the coating cracks were still found arrested at the coating/substrate interface, Fig. 12e; and the distance between the coating cracks further reduced to  $43.27 \pm 11.84 \mu\text{m}$ .

Crack patterns of the PVD sample S7 tested at  $345^\circ\text{C}$  and imaged by SEM are shown in Fig. 13a. Similar to the PVD materials tested at RT, a cross-sectional view (Fig. 13a) showed that these coating cracks did not penetrate into the substrate. Compared to the coating cracks at RT which formed (of the Y-Z plane) at an angle range of  $80^\circ$  to  $105^\circ$  to the hoop direction, some cracks in the coating surface at  $345^\circ\text{C}$  were found to form at a larger angle ( $75^\circ$  to  $109^\circ$ ) to the hoop direction (the maximum angle between coating cracks is  $\sim 34^\circ$ , Fig. 13b). These are all consistent with the findings by *in situ* XCT imaging, Fig. 12. Magnified SEM images revealed these coating cracks mostly propagated intergranularly, with an almost doubled crack width (1–8  $\mu\text{m}$ ) compared to that (1–4  $\mu\text{m}$ ) at RT (Fig. 13c–e). As shown by the SEM images, toughening mechanisms again included parallel cracks (Fig. 13c), bifurcation (Fig. 13d) and

### 345°C Failure Process of Cold Sprayed Cr-coated Materials

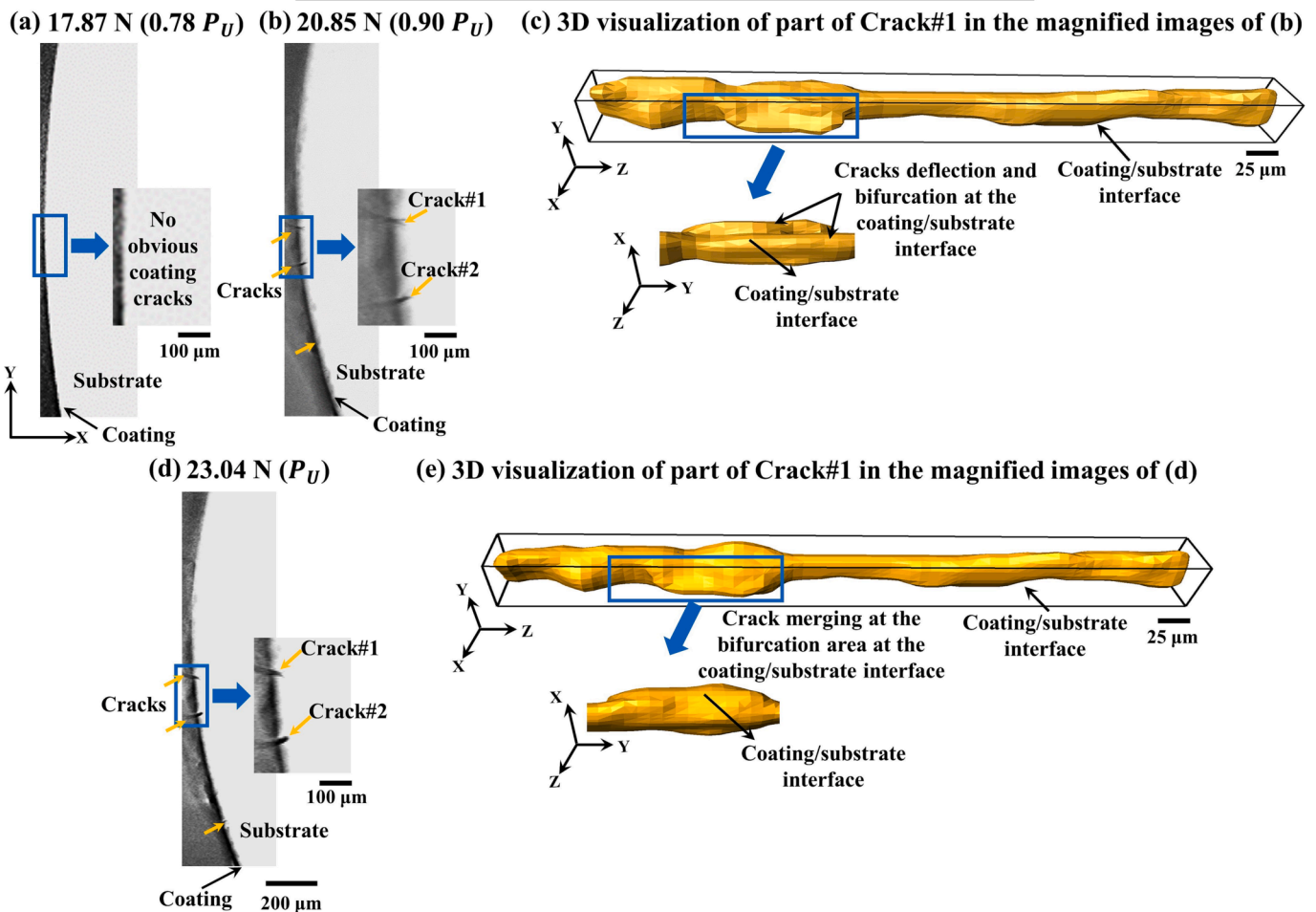


**Fig. 8.** (a), (b) and (d) are *in situ* XCT slices of the X-Y plane (including magnified images extracted from the same location in the sample at increasing loading steps) showing crack formation and propagation processes of the cold sprayed (CS) Cr-coated materials tested at 345 °C, from sample S3: (a) scan at 17.87 N (0.78  $P_U$ ) before peak load with no obvious coating cracks, (b) scan at 20.85 N (0.90  $P_U$ ) before peak load at where three simultaneous coating cracks were initially formed and imaged by XCT, (d) scan at peak load 23.04 N ( $P_U$ ). (c) and (e) are 3D visualization of part of the representative coating crack (Crack#1, selected range in a length of ~ 460  $\mu\text{m}$ , which is ~ 21% of the total sample's width: ~2.2 mm) in the magnified images of (b) and (d) respectively. (c) shows crack deflection and bifurcation at the coating/substrate area in some parts of Crack#1, (e) shows crack merging at the bifurcation area at the coating/substrate interface of Crack#1 with further loading.

deflection (Fig. 13e), with uncracked ligament bridging observed to be either at the bifurcation areas (Fig. 13d) or within the cracks (Fig. 13e).

To summarize, for PVD Cr-coated materials tested at both RT and 345 °C, multiple coating cracks formed simultaneously at ~ 80% peak load in the Cr coating. No evidence revealed that these cracks penetrated the substrate after reaching peak load. At both RT and 345 °C, once coating cracks formed, the majority of them tended to travel across the sample's total width; further loading led to the formation of new coating cracks, as well as further extended in length of the semi-across width cracks formed at previous loading stages. At RT, the cracks were at a width of 1–4  $\mu\text{m}$  at the coating surface and formed almost vertically (at an angle of 80° to 105°) to the hoop direction of the sample. However, at 345 °C, the coating cracks displayed a larger width (1–8  $\mu\text{m}$ ), as well as a larger angle range (75° to 109°) from the tensile hoop direction. No coating spallation was found at either temperature.

## 4. Discussion

### 4.1. Microstructures and local properties of CS and PVD Cr-coated materials

The tortuous Cr coating/substrate interface in the CS Cr-coated

material is a typical morphology of the cold spraying process [3,4]. The thickness of these coatings can be quite varied, as also observed by Fazi *et al.* [4]. Small pores distributed in the CS coating in optical images (Fig. 2a) were confirmed by band contrast EBSD maps in Fig. 3a. These are attributed to the deposition process of the CS method, and are commonly found between former Cr powder particles [4,11]. Fazi *et al.* [11] pointed out that as these small pores are isolated from outer environment, they have a negligible effect on the coating oxidation resistance. To be noted that, the high interfacial roughness and the splated Cr grains in the coating could potentially affect the crack pathways in the coating and hoop strength when first coating cracks being observed, with detailed discussions presented in Section 4.2.

Compared to CS Cr-coated materials, the PVD Cr coating/substrate interface was found to be smoother (Fig. 2b), with the coating almost fully dense with no obvious porosity (Fig. 3b). The Cr grains were columnar in shape, with a strong texture along [1 1 1] direction in both hoop and axial direction, with smaller grains at the coating/substrate interface, consistent with typical PVD coatings reported in the literature [15]. The PVD Cr grains were often observed to exhibit either, or both, strong [1 1 0] and [1 1 1] crystallographic textures with direction normal to the deposition surface [15,16,36]. It is noticeable that the columnar Cr grains in the PVD coating could affect the pathways of coating cracks,

## 345°C Crack Patterns of Cold Sprayed Cr-coated Materials

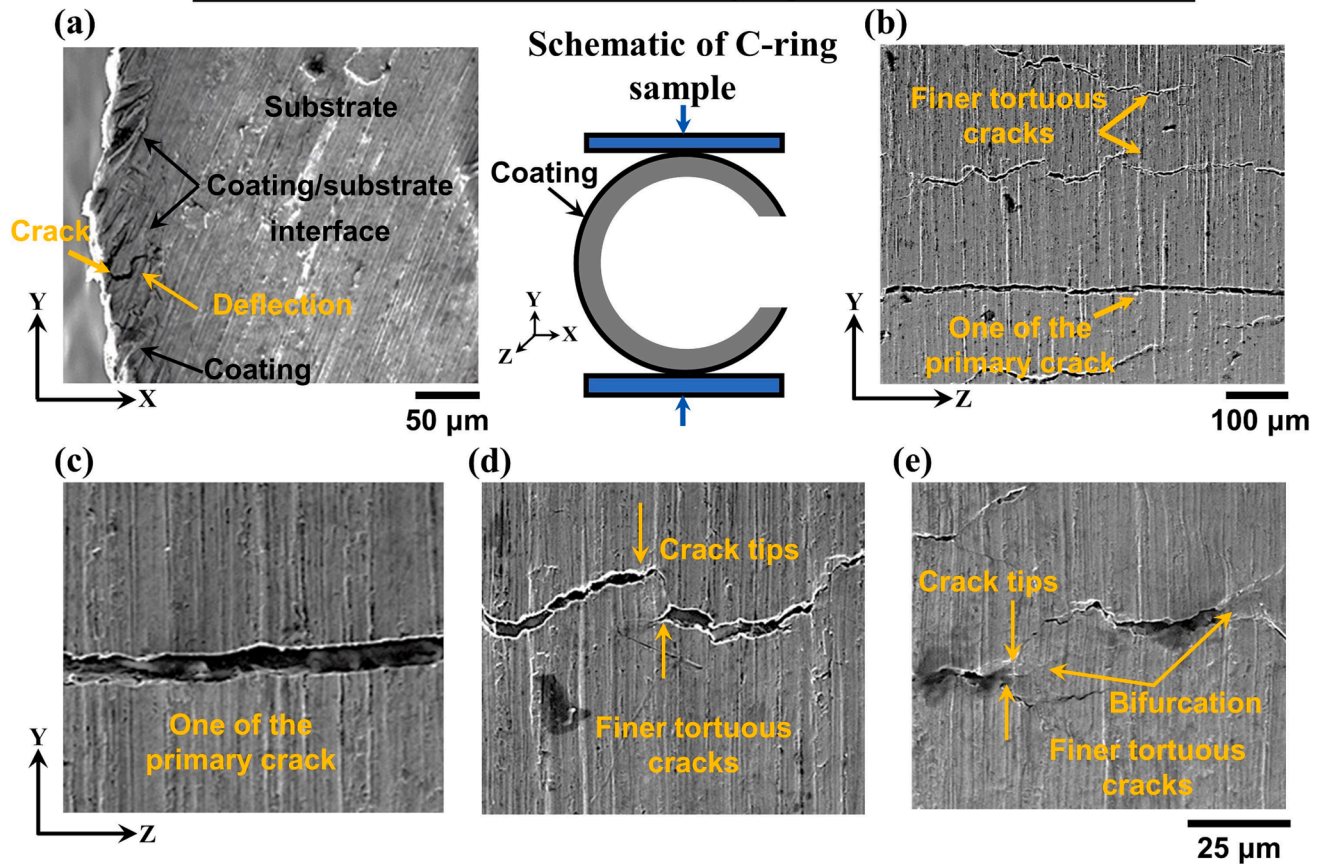


**Fig. 9.** SEM images showing crack patterns of the post-failure cold sprayed (CS) Cr coated materials tested at 345 °C, from sample S3: (a) image collected from the side surface of sample (of the X-Y plane) showing one of the primary coating cracks, which did not penetrate through to the underlying substrate, with crack deflection observed in the coating; (b) low magnification view from the outer surface at the sample's middle plane (of the Y-Z plane) showing multiple cracks, including one of the primary crack formed perpendicular to the tensile hoop direction of the sample; the others are finer tortuous cracks. (c) to (e) are high magnification views of the outer surface of the sample (of the Y-Z plane), including one of the primary cracks and finer tortuous cracks: (c) shows the primary crack formed vertical to the tensile hoop direction without any deflection or bifurcation being observed within the crack; (d) shows crack deflection at the tips of finer tortuous cracks and (e) shows crack bifurcation at the tips of finer tortuous cracks. One schematic of C-ring sample with loading is included.

as well as the strength when coating cracks firstly being observed, as discussed in detail in Section 4.2. In addition, due to these larger columnar Cr grains, the average size of the Cr grains in the PVD coating (with an area of  $0.39 \pm 1.22 \mu\text{m}^2$ ) was about 1.4 times higher than that in the CS coating ( $0.16 \pm 0.42 \mu\text{m}^2$ ).

Literature values of the hardness and elastic modulus of the Cr coating and Zircaloy substrate [37] are reviewed and listed in Table S4 in the Supplementary Materials. Specifically, the hardness and modulus of Cr coatings are respectively in the range of 2.9 to 14.2 GPa and 140–300 GPa; corresponding values for the Zircaloy substrate are typically 1.8–3.0 GPa and 95–115 GPa. The results of the current study are consistent with these values.

For CS Cr-coated materials, the local properties of both the coating and substrate were found to become significantly varied close to the interface. Specifically, for the coating, the hardness of Area #1 (~4.5 GPa) was ~ 18.4% higher than that in Area #2, ~ 3.8 GPa. As for the substrate, the hardness of Area #3 (~3.0 GPa) was ~ 15.3% higher than in Area #4 (~2.6 GPa). Similar trends have been reported by Fazi *et al.* [11] in a CS Cr-coated ZIRLO™ cladding material, although no exact values of the modulus and hardness were presented. The nanoindentation hardness measured in the middle of their Cr coating (at a location similar to those tested in Area #1 in current work) was ~ 27.8% higher than that measured at locations close to the interface (at a location similar to those tested in our Area #2). Similarly, the hardness of the substrate close to the interface, *i.e.*, within 5 μm (at a location akin

to our Area #3) was ~ 40% higher than that measured in the substrate away from the interface (detailed results of their measurements are presented Fig. S3 in the Supplementary Materials). During the CS process, Cr and Zr elements could diffuse into each other over a distance of ~ 40 nm, and generate an intermixed bonding region at the interface (see example in Fig. S4) [11]. In current work, the nanoindentation tests performed in the substrate were ~ 3 μm to ~ 5 μm away from the interface (far away from the such intermixed bonding region (element diffusion region)), therefore the influence of such intermixed bonding region to the variation of local properties could be considered negligible. As such the variations in measured data were most likely the result of plastic deformation in the coating and substrate close to the interface during the manufacturing process [11], which can cause deformed and elongated Cr grains [38,39], smaller grain sizes and a higher dislocation concentration in the substrate near the interface. Such plastic deformation during CS coating manufacturing could also impact its interfacial toughness. This is discussed below in Section 4.3.

For PVD Cr-coated materials tested in the current study, the hardness of Area #2 (~5.2 GPa) is also higher (by about 16%) than Area #1 (~4.5 GPa). This is attributed to the smaller size of the Cr grains located close to the interface (Fig. 3b), which is typical for PVD Cr coatings [40]. In contrast to the CS materials, there is no significant variation in hardness in the substrate of PVD materials as the PVD process does not lead to any plastic deformation.

### Room Temperature Failure Process of Physical Vapour Deposited Cr-coated Materials

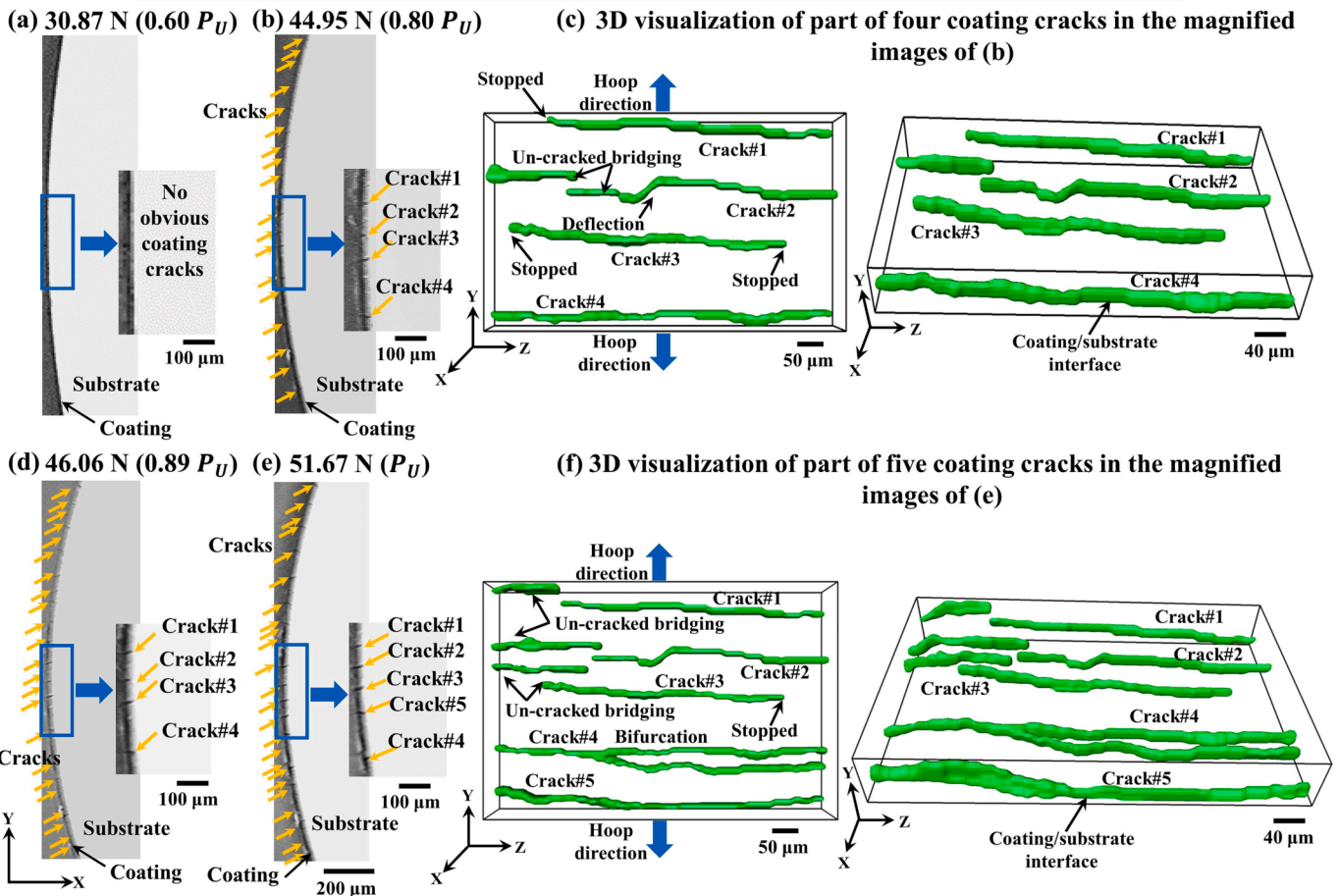


**Fig. 10.** (a), (b), (d) and (e) are *in situ* XCT slices of the X-Y plane (including magnified images extended from the same location in the sample at increasing loading steps) showing crack formation and propagation processes in the physical vapour deposited (PVD) Cr-coated materials tested at RT, from sample S5: (a) scan at 30.87 N (0.60  $P_U$ ) before peak load with no obvious coating cracks, (b) scan at 44.95 N (0.80  $P_U$ ) before peak load where simultaneous coating cracks were first formed and imaged by XCT, (d) scan at 46.06 N (0.89  $P_U$ ) before peak load, and (e) scan at peak load 51.67 N ( $P_U$ ). (c) and (f) are 3D visualization of part of the representative coating cracks (selected range in a length of  $\sim 540 \mu\text{m}$ , which is  $\sim 22\%$  of the total sample's width:  $\sim 2.5 \text{ mm}$ ) in the magnified images of (b) and (e) respectively. (c) shows Crack#1 to Crack#4 at 44.95 N (0.80  $P_U$ ) before peak load; Crack#1 and Crack#3 stopped in the coating without travelled across the sample's total width; Crack#2 and Crack#4 travelled across the sample's total width with deflection and uncracked bridging being observed in Crack#2. (f) shows the formation of Crack#5 at peak load 51.67 N ( $P_U$ ), Crack#1 and Crack#3 extended further in length with un-cracked bridging, and a new crack branched out from Crack#4.

#### 4.2. Strength of the CS and PVD Cr-coated cladding materials at RT and 345 °C

Using various testing methods, such as plug-expansion, uniaxial tension and tensile tests, the room temperature maximum hoop strength of similar CS and PVD Cr-coated Zircaloy materials have been reported in the open literature to be in the range of  $\sim 400 \text{ MPa}$  to  $\sim 1322 \text{ MPa}$  [13,15,16,40,41]; a detailed summary of these values is presented in Table S5 in the Supplementary Materials. In the present study, the maximum hoop stresses at RT are  $\sim 1168 \text{ MPa}$  and  $\sim 1150 \text{ MPa}$  respectively for the CS and PVD Cr-coated materials. Although such calculated maximum hoop stresses are approximate values based on Eq. (4), they are still in the reported range. In this work, the estimated maximum hoop stresses tested at 345 °C for both types of cladding materials were all found to be lower than those at RT by  $\sim 50\%$ ; with  $\sim 631 \text{ MPa}$  ( $\sim 54\%$  of RT value) for CS Cr-coated materials, and  $\sim 611 \text{ MPa}$  ( $\sim 53\%$  of RT value) for PVD Cr-coated materials. Similar phenomena have been reported by Roache *et al.* [13,41] on their CS Cr-coated Zircaloy cladding materials, tested at both RT and 315 °C using a plug-expansion test. The maximum hoop stresses of samples tested at 315 °C ( $\sim 500 \text{ MPa}$ ) were 60% to 70% of the RT values (700–800 MPa). Jiang *et al.* [16] also reported the tensile strength at 350 °C ( $\sim 240 \text{ MPa}$ )

of their PVD Cr-coated Zircaloy sheet samples as  $\sim 55\%$  of the strength tested at RT ( $\sim 440 \text{ MPa}$ ). These are all consistent with the findings in present work suggesting that the C-ring compression test is comparable with other test configurations.

In current study, the hoop strength of the first formation of coating cracks of CS coating was  $\sim 1020 \text{ MPa}$  at RT and  $\sim 584 \text{ MPa}$  at 345 °C, which were respectively 13.7% and 14.5% higher than the PVD coating ( $\sim 897 \text{ MPa}$  at RT and  $\sim 510 \text{ MPa}$  at 345 °C). Note that the accurate strength of first coating cracks' formation of CS materials at 345 °C could lower than  $\sim 584 \text{ MPa}$ , as finer coating cracks (Fig. 9) could form prior to the primary coating cracks and were not detected by XCT imaging. Similar phenomenon has been reported by Burden *et al.* [14] from their CS ( $\sim 25 \mu\text{m}$  in thickness) and PVD ( $\sim 20 \mu\text{m}$  in thickness) Cr-coated Zircaloy cladding tube materials under C-ring compression at RT. Although no exact stress values were reported, the coating crack initiation point (captured by real-time SEM imaging) for their CS materials is  $\sim 10.5 \text{ N/mm}$ , which is  $\sim 23.5\%$  higher than that of PVD materials ( $\sim 8.5 \text{ N/mm}$ ). Additionally, from the reported cross-sectional SEM images of the post-tested samples, compared with the cleavage crack behaviours of PVD coating (cracks travelled along the boundaries of columnar grains, which served as a smoother crack pathways, see example in Figs. S5a and S5b in the Supplementary Materials), the

### Room Temperature Crack Patterns of Physical Vapour Deposited Cr-coated Materials

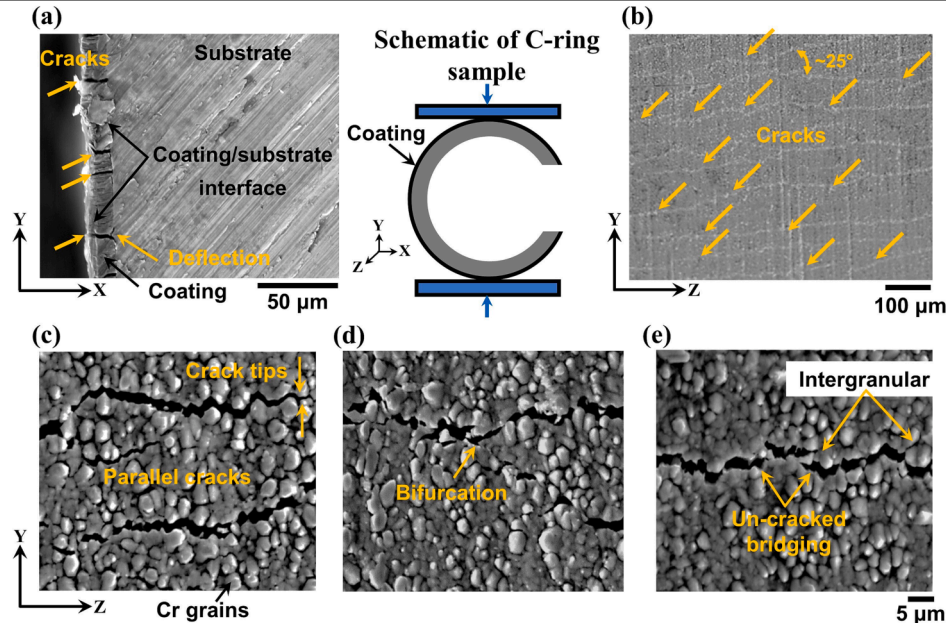


**Fig. 11.** SEM images showing crack patterns of the post-failure physical vapour deposited (PVD) Cr-coated materials tested at RT, from sample S5: (a) image collected from the side surface of sample (of the X-Y plane) shows cracks do not penetrate through to the underlying substrate with crack deflection observed along the coating/substrate interface; (b) low magnification view of the outer surface of the sample (of the Y-Z plane) shows multiple cracks formed almost perpendicular (in the angle range of  $80^\circ$  to  $105^\circ$ ) to the tensile hoop direction of the sample, with the maximum angle between coating cracks is  $\sim 25^\circ$ ; (c) to (e) are high magnification views of the outer surface of the sample (of the Y-Z plane): (c) shows parallel cracks and cracks deflected along the Cr grain boundaries; (d) shows crack bifurcation and (e) uncracked ligament bridging, with most cracks in an intergranular mode. One schematic of C-ring sample with loading is included.

pathways of CS coating cracks were more torturous as they travelled along the individual splatted grain boundaries, enabled them to be more potentially to be arrested and deflected prior to reach the interface and generate large cracks (see example in Fig. S5c) [14]. Such crack deflection in the CS coating was also observed in current work, see example in Fig. 9a. Additionally, as suggested by Burden *et al.* [14], the high roughness of CS coating/substrate interface resulted in a strong mechanical interlocking of the coating and substrate increasing the complexity of load redistribution. Therefore, in current study, the potential reasons for the higher strength (first coating cracks' formation) of CS coating (compared with PVD coating) could be attributed to splatted grains in the coating and its higher interfacial roughness.

#### 4.3. Interfacial toughness, failure process and crack patterns of CS and PVD materials

##### 4.3.1. Interfacial failure mode and estimation of interfacial toughness at room temperature

In this work, for CS and PVD Cr-coated materials tested at both RT and  $345^\circ\text{C}$ , once coating cracks reached the coating/substrate interface, they were arrested or deflected at the interface without penetrating the underlying substrate; this was confirmed both by XCT and SEM imaging. One typical example is presented in Fig. 11a, from the SEM image of the side surface (X-Y plane) of a sample after failure, where some doubly deflected cracks can be observed along the interface for the PVD material tested at RT. As no obvious coating spallation was found for the CS and PVD materials tested at both RT and  $345^\circ\text{C}$ , there was clearly good adhesion of the Cr coating to the substrate. This is consistent with observations reported by Roache *et al.* [13,41] on CS Cr-coated Zircaloy cladding tubes under plug-expansion tests at RT and  $315^\circ\text{C}$ , and by Jiang *et al.* [16] on PVD Cr-coated ( $\sim 15\ \mu\text{m}$  of coating thickness) Zircaloy sheet samples ( $20 \times 3 \times 0.6\ \text{mm}^3$ ) under tensile tests from RT to  $500^\circ\text{C}$ .

As the local modulus of the coatings and substrate were measured in the present study, with the mode I fracture toughness or strain energy

release ( $K_{Ic}$  or  $G_{Ic}$ ) of Zircaloy cladding material known, the upper bound of the mixed mode coating-substrate interfacial fracture toughness or strain energy release rate ( $G_{ic}$ , including singly interfacial deflected cracks and doubly interfacial deflected cracks) at room temperature can be determined from the He and Hutchinson method based on first Dundurs parameter ( $\alpha$ ) [42,43], assuming largely elastic conditions (Fig. 14). As a coating crack approaches and impinges on the coating/substrate interface, it can penetrate the underlying material (Fig. 14a) or become arrested at the interface with either a single-side (Fig. 14b) or double-side interfacial deflection (Fig. 14c). Fig. 11a presents an example for the situation described in Fig. 14c for a nominally perpendicular impingement. The first Dundurs parameter ( $\alpha$ ) represents the elastic modulus mismatch across the interface of two dissimilar materials (details on this can be seen in refs [42,43]), and is defined by:

$$\alpha = \frac{E'_1 - E'_2}{E'_1 + E'_2} \quad (7)$$

where  $E'_1$  and  $E'_2$  are the plane-strain elastic modulus of the Zircaloy and Cr, respectively, as can be calculated from:

$$E'_i = \frac{E_i}{1 - \nu_i^2} \quad (8)$$

where  $E_i$  and  $\nu_i$  are the elastic modulus and Poisson's ratio of the corresponding material, respectively. The critical strain energy release rate,  $G_{Ic}$ , can be correlated to the critical stress intensity  $K_{Ic}$  by assuming primarily mode I cracking:

$$G_{Ic} = \frac{K_{Ic}^2}{E_1} \quad (9)$$

where  $E_1$  is the elastic modulus of Zircaloy substrate close to the interface. Eq. (9) is used to convert the literature reported Zircaloy mode I fracture toughness to critical strain energy release rate to correlate the mixed-mode interfacial toughness,  $G_{ic}$ , using the first Dundurs parameter,  $\alpha$  (Eq. (7)).

### 345°C Failure Process of Physical Vapour Deposited Cr-coated Materials

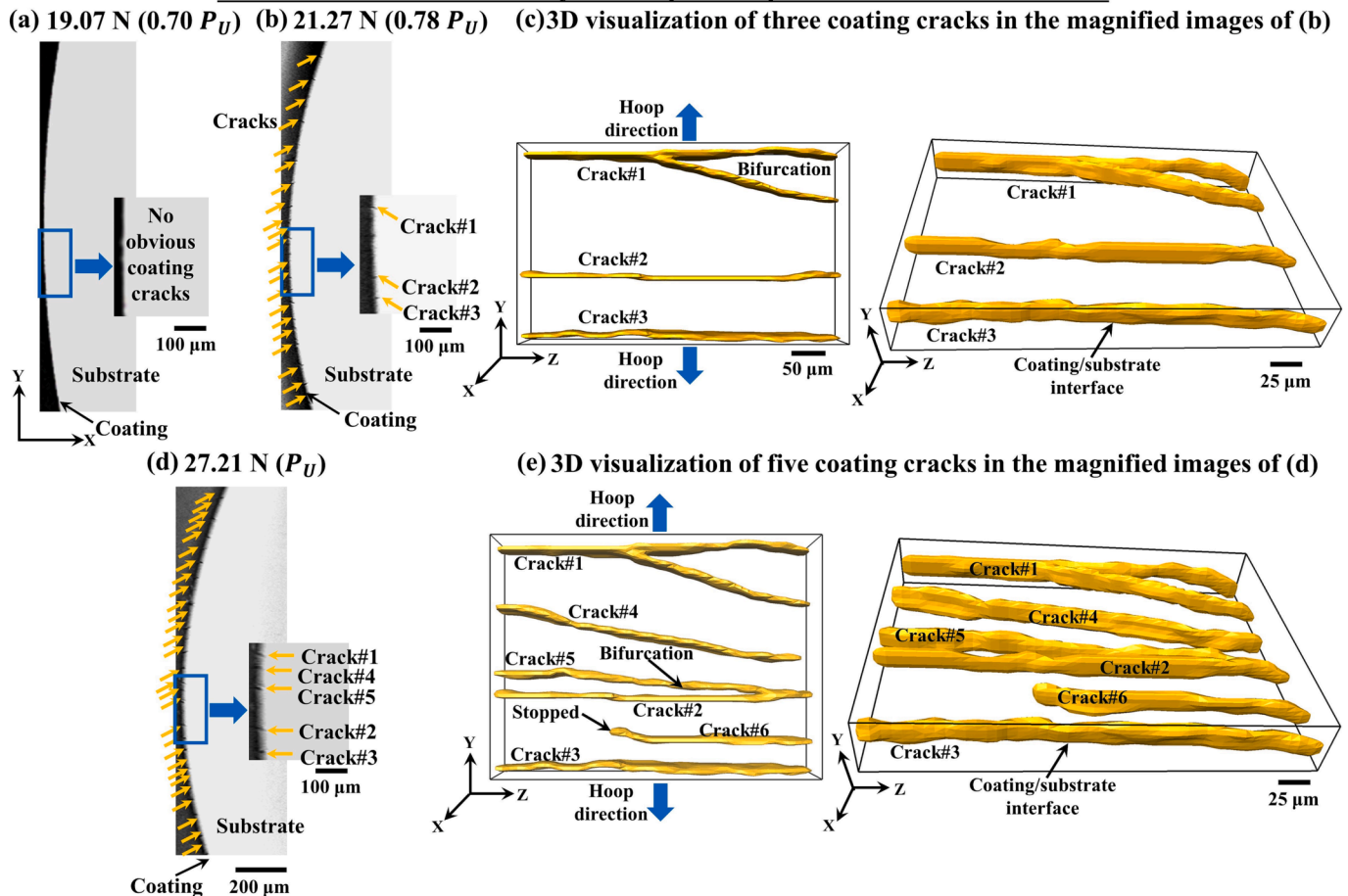


**Fig. 12.** (a), (b) and (d) are *in situ* XCT slices of the X-Y plane (including magnified images extracted from the same location in the sample at increasing loading steps) showing crack formation and propagation processes in the physical vapour deposited (PVD) Cr-coated materials tested at 345 °C, from sample S7: (a) scan at 19.07 N (0.70  $P_U$ ) before peak load with no obvious coating cracks, (b) scan at 21.27 N (0.78  $P_U$ ) before peak load where simultaneous coating cracks were first formed and imaged by XCT, (d) scan at peak load 27.21 N ( $P_U$ ). (c) and (e) are 3D visualization of part of the representative coating cracks (selected range in a length of  $\sim 450$   $\mu\text{m}$ , which is  $\sim 19\%$  of the sample's total width:  $\sim 2.4$  mm) in the magnified images of (b) and (d) respectively. (c) shows Crack#1 to Crack#3 at 44.95 N (0.80  $P_U$ ) before peak load; they all travelled across the sample's total width with bifurcation being observed in Crack#1. (e) shows Crack#1 to Crack#6 at peak load 27.21 N ( $P_U$ ). Noted that the newly formed Crack#6 did not travel across the sample's total width, and not being observed in the selected magnified image in Fig. 12d.

Ren [44] used a modified Vallecitos embedded Charpy (VEC) technique to acquire the mode I stress-intensity factor,  $K_{Ic}$ , of Zircaloy-4 (similar type of substrate material with current work) cladding tube materials at RT. The geometry of the cladding tube ( $r_o$  being  $\sim 4.7$  mm and  $r_i$  being  $\sim 4.1$  mm) in their work is also similar to that of current study ( $r_o$  being  $\sim 4.6$  mm and  $r_i$  being  $\sim 4.0$  mm). The reported  $K_{Ic}$  (101.1 MPa/ $\text{m}^2$  at RT) [44] is therefore selected to estimate the interfacial toughness  $G_{ic}$ . Using Eq. (9), the converted critical strain energy release rate for the substrate of CS and PVD Cr-coated materials were calculated to be 93.33 J/ $\text{m}^2$  and 90.13 J/ $\text{m}^2$ , respectively. By inputting the measured elastic modulus of the coating and substrate close to the interface (Areas #2 and 3, Table 2) of both CS and PVD materials, the first Dundurs parameter ( $\alpha$ ) for singly and doubly deflected interfacial cracks, and corresponding upper-bound of interfacial toughness ( $G_{ic}$ ) were calculated, as listed in Table 4.

Based on Fig. 14d, both the CS and PVD Cr-coated materials tested at RT were investigated. For interfacial crack deflection, the first Dundurs parameter ( $\alpha$ ) is  $-0.37$ , such that the interfacial toughness ( $G_{ic}$ ) should be respectively more than 0.24 and 0.12 times that of the Zircaloy for both singly and doubly interfacial crack deflection. It can be found the upper bound of the interfacial toughness ( $G_{ic}$ ) at RT for single (22.39 J/ $\text{m}^2$ ) and doubly (11.20 J/ $\text{m}^2$ ) deflected cracks of the CS materials are both  $\sim 3.6\%$  higher than that for the PVD materials (21.62 J/ $\text{m}^2$  and

10.81 J/ $\text{m}^2$ ). It is suggested that the higher interfacial toughness for the CS materials could result from the relatively strong interfacial locking of the coating and substrate [3], caused by plastic deformation close to the interface area during the CS manufacturing process [11].

#### 4.3.2. Failure processes and crack patterns of CS and PVD materials at RT and 345 °C

In this work, for both the CS and PVD Cr-coated cladding materials tested at RT and 345 °C, the formation and progressive development of coating cracks were successfully imaged by *in situ* XCT imaging. More importantly, the XCT slices (2D images and 3D reconstructed slices) presented in current work provided crack pathways in the coating; such information could not be offered by 2D SEM images, as SEM only provides information of either the surface of coating cracks or the coating cracks at the cross-sections at sample's edge. These all demonstrated the current resolution of XCT images (3.25  $\mu\text{m}/\text{pixel}$ ) is sufficient to provide the crack information in the Cr coating. It is noticeable that the reconstructed XCT images are greyscale images with different contrast represents the variation of X-ray attenuation of various phases within a specimen. However, in current work, all the Cr grains in the Cr coating have the body-centred cubic (bcc) structures; therefore, from the XCT imaging, each grain in the Cr coating cannot be distinguished and no information of internal material structure could be presented. Future

**345°C Crack Patterns of Physical Vapour Deposited Cr-coated Materials**

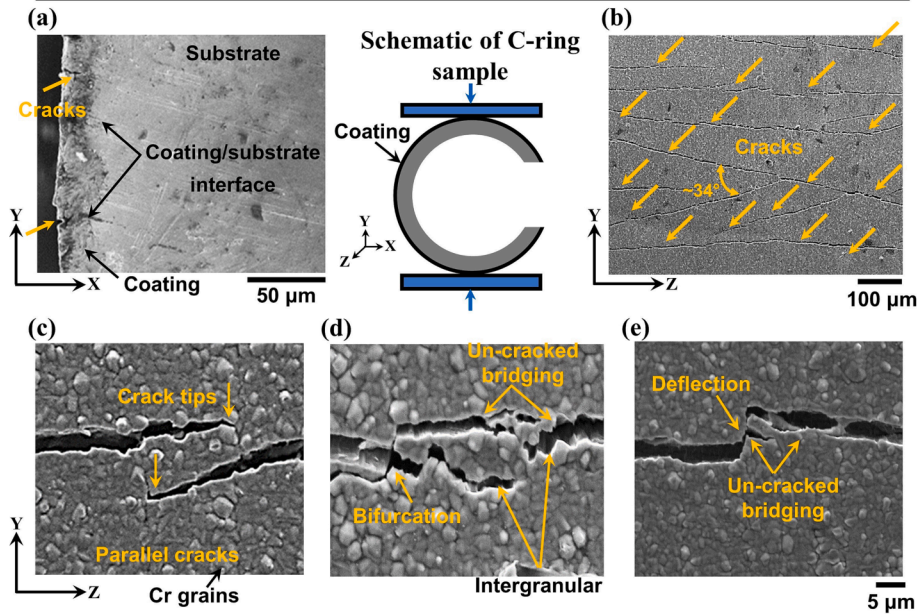


**Fig. 13.** SEM images showing crack patterns of the post-failure physical vapour deposited (PVD) Cr coated materials tested at 345 °C, from sample S7: (a) image collected from the side surface of sample (of the X-Y plane) shows they do not penetrate through to the underlying substrate; (b) low magnification view of the outer surface of the sample (of the Y-Z plane) shows multiple cracks, with most cracks formed perpendicular to the tensile hoop direction of the sample, and some cracks formed with an angle (in the range of 75° to 109°) against the tensile hoop direction, with the maximum angle between coating cracks is ~ 34°; (c) to (e) are high magnification views of the outer surface of the sample (of the Y-Z plane): (c) shows parallel cracks and crack deflection at the crack tips along the Cr grain boundaries; (d) shows crack bifurcation at the uncracked ligament bridging area; (e) shows crack deflection within the crack. One schematic of C-ring sample with loading is included.

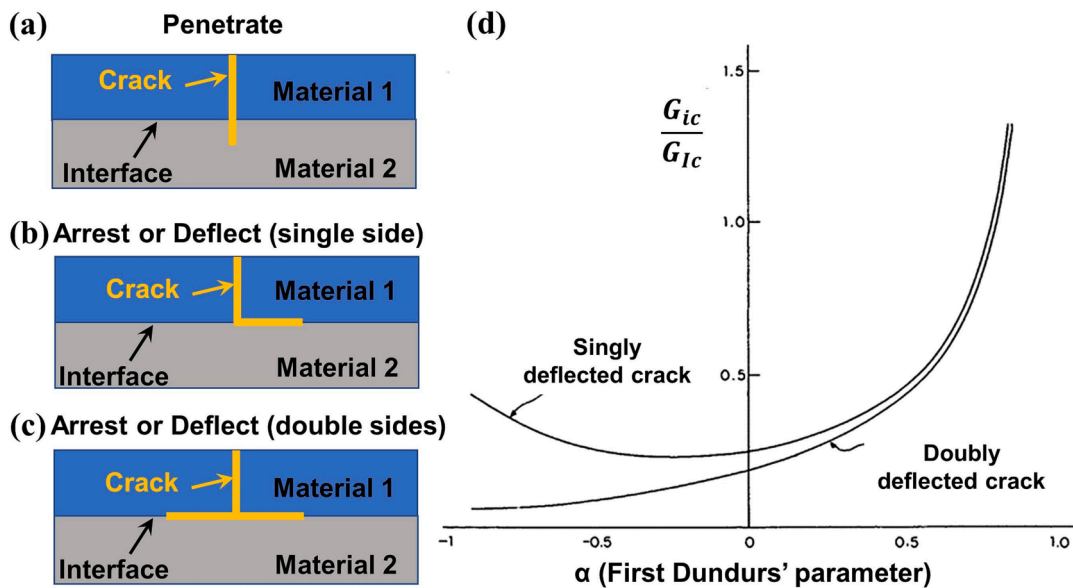


**Fig. 14.** Schematic illustrations to demonstrate when a crack runs from material 1 and impinges on the interface with a dissimilar material 2, it can have three ways to propagate: (a) penetrate the substrate (material 2), (b) arrest or with single-side deflection or (c) arrest or with double-side deflection. (d) Diagram of He and Hutchinson's linear-elastic analytical solution [42,43], once a crack in one material impinges the interface with a different material, the behaviour of crack (including penetrates, arrests, deflects in either single-side or double-side) is a function of the elastic modulus mismatch across the interface. As is defined by the interfacial toughness,  $G_{ic}$ , the critical strain energy release rate,  $G_{Ic}$ , of material 2 (Zircaloy substrate) and the first Dundurs parameter ( $\alpha$ ).

EBSM mapping on the crack areas of post-tested samples could be conducted, aiming at investigating the relation between crack pathways and the orientation of Cr grains in the coating.

Compared with the Zircaloy substrate (~650 μm in thickness), although the coating is thin (around 10 to 20 μm in thickness), both the application of Cr coating and the formation and propagation of coating

cracks could affect the mechanical properties of the entire cladding system. For example, Kim *et al.* [23] conducted ring compression tests on two types (with different coating thickness: ~8.3 μm and ~ 18.8 μm) of PVD Cr-coated Zircaloy cladding tube materials at RT. It can be found, even the application of a thin (~8.3 μm in thickness) PVD Cr coating could significantly affect the load–displacement curve, as obvious load

**Table 4**

Calculated first Dundurs parameter ( $\alpha$ ), as well as corresponding upper bound of the interfacial toughness ( $G_{ic}$ ) for the situations of singly and doubly deflected interfacial cracks of both CS and PVD Cr-coated Zircaloy cladding tube materials tested at RT.

Deflection types	CS		PVD	
	$\alpha$	$G_{ic}(\text{J/m}^2)$	$\alpha$	$G_{ic}(\text{J/m}^2)$
Singly deflected cracks	-0.37	22.39	-0.37	21.62
Doubly deflected cracks		11.20		10.81

drops were observed when the applied displacement reach to 6 mm, and the magnitude of the load drop increasing with coating thickness, see Fig. S6 in the Supplementary Materials. They suggested that [23], under loading, cracks initially formed across the coating thickness and acts as a pre-existing flaw that concentrates stresses, growing towards the underlying substrate. Once the crack growing depth reaching the critical size, it unstably grows up and finally leads to the failure of the entire coated cladding system, present as the early load drop in curves compared to the uncoated materials (Fig. S6). Additionally, the formation of coating cracks could also affect the acoustic energy (AE) signals. Roache *et al.* [13,41] performed plug-expansion tests on CS Cr-coated Zircaloy cladding tube materials, and AE was adopted to identify the formation and propagation of coating cracks. They reported that the initial sharp rise in AE activity was caused by crack initiation around the circumference of the sample, see Fig. S7. These all indicated that, although the coating is thin, its unignorably influences to the stress-strain behaviours of the entire Cr-coated Zircaloy cladding materials should be thoroughly investigated for their future industrial application.

For the CS materials tested at RT, multiple coating cracks formed at ~ 90% of the peak load (Fig. 6), with the distance between the coating cracks steadily decreasing with increasing load, from  $98.89 \pm 34.71 \mu\text{m}$  to  $58.38 \pm 17.21 \mu\text{m}$  at peak load; this is summarised in Fig. 15a. These cracks were found to be nearly perpendicular to the hoop direction (Fig. 7), indicating that the hoop stress is the main contributor to the coating fracture at RT. Some crack toughening mechanisms (*e.g.*, crack deflection and bifurcation) were observed for the CS coating cracks, Fig. 6e and Fig. 7. Similar phenomenon was also reported by Roache *et al.* [13,41] (under plug-expansion tests at RT) and Burden *et al.* [14] (under C-ring compression tests at RT) of their CS Cr-coated Zircaloy cladding tube materials; and one potential reason is that when coating cracks travelled along the boundaries and gaps between the splatted Cr grains in the CS coating, enabled them have more potentials to transfer their growth paths away from the direction (hoop direction in current work) of maximum driving force [14]. At some crack tips, cracks

deflections along the striations in the coating (~90° to the crack length) were observed (Fig. 7a) but they did not have any major impact to the overall crack direction patterns. The failure process of the CS Cr-coated cladding materials tested at RT can be classified into three stages: (i) initial collective deformation in the coating/substrate system without crack formation; (ii) multiple coating cracks formed simultaneously at ~ 90% of peak load oriented perpendicular to the tensile hoop direction with toughening mechanisms presented; (iii) with increasing load, the distance between the coating cracks steadily decreased to about 60% of the initial distance at formation when reaching peak load.

However, for the CS Cr-coated cladding materials tested at 345 °C, in addition to the three primary cracks (vertical to the hoop direction), tortuous small cracks (finer in width) were also observed (Fig. 7); as discussed in Section 3.4.1, these finer cracks were likely formed prior to the primary cracks. Such tortuous fine coating cracks were also reported on CS Cr-coated Zircaloy cladding tubes under plug-expansion tests at 315 °C [13,41] with angles oriented at ~ 65° to 75° to the axial direction. From their FEA analysis [13], tensile residual strains between Cr coating and Zircaloy substrate were measured at both axial (0.026%) and circumferential (0.031%) directions (as been presented in Fig. S8 and Fig. S9 in the Supplementary Materials, respectively), caused by the thermal expansion mismatch of Cr ( $4.9$  to  $8.2 \times 10^{-6}/^\circ\text{C}$  [45,46]) and Zircaloy substrate ( $6.6 \times 10^{-6}/^\circ\text{C}$  [47,48]) when temperatures rising from RT to 315 °C. It was suggested that such tensile residual strains could create a shear stress state predisposed to off axis cracking and generate a multi-dimensional stress-state in the coating [13], which led to the tortuous small coating cracks in current work. As with increasing load, the tensile hoop stress generated in C-ring compression will exceed the thermal multi-dimensional stresses [13], this is considered to be a potential reason for the two-stages of crack formation observed in the present work: (i) the formation of finer coating cracks in the first stage caused by multi-dimensional stresses from the thermal mismatch, and (ii) the formation of primary cracks caused by the tensile hoop stress in the second stage. Note that the number of primary cracks did not increase with increasing load, which is very different from behaviour at RT, as illustrated in Fig. 6. Accordingly, the failure processes in the CS Cr-coated cladding materials tested at 345 °C can be classified into four stages: (i) initial collective deformation in the coating/substrate system without crack formation; (ii) formation of finer tortuous coating cracks due to the multi-directional stress distribution upon heating with a low hoop stress; (iii) with increasing tensile hoop stress, several straight primary coating cracks (vertical to hoop direction) form at ~ 90% of peak load; (iv) with further loading the number of primary cracks did not increase but their width did.

For PVD materials tested at RT, multiple coating cracks formed

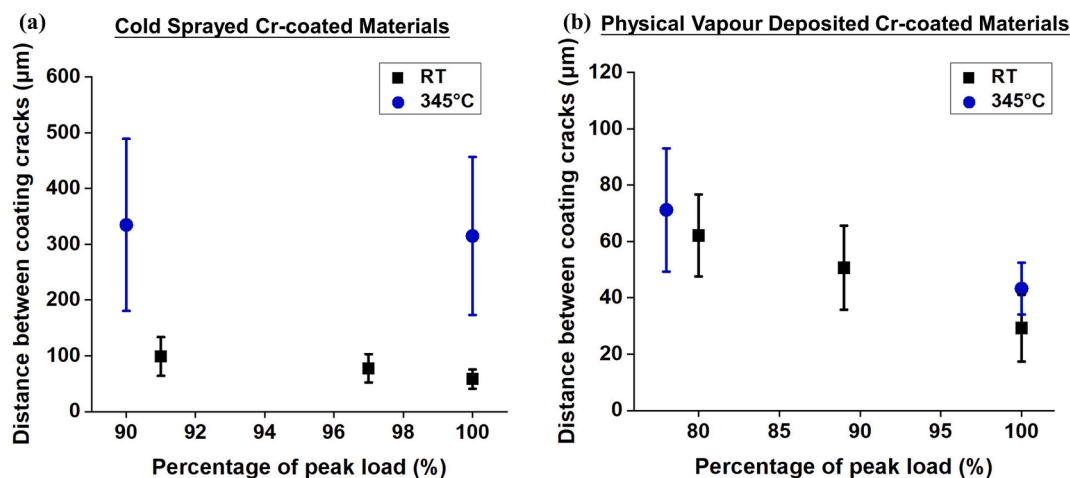


**Fig. 15.** Distance between the coating cracks measured by real-time XCT imaging at increasing loading stages for the Cr-coated cladding materials using both CS and PVD methods for tests at both room temperature and 345 °C: (a) cold sprayed Cr-coated materials and (b) physical vapour deposited Cr-coated materials.

simultaneously at 80% of peak load, with the distance between the coating cracks steadily decreasing, from  $62.13 \pm 14.55 \mu\text{m}$  to  $29.27 \pm 11.84 \mu\text{m}$  at peak load (Fig. 15b). Note the distance between coating cracks (upon formation as well as with increasing load) were much smaller than with the cold sprayed materials (Fig. 15). These coating cracks were almost perpendicular to the tensile hoop stress (in an angle range of  $80^\circ$  to  $105^\circ$ ) and propagated mostly in an intergranular manner (Fig. 11). For the PVD materials tested at  $345^\circ\text{C}$ , the distance between the coating cracks (from formation to peak load) was similar to that at RT – this is very different from the cold sprayed materials where a much larger distance between the primary cracks was observed at  $345^\circ\text{C}$  than at RT. There are three more main differences of the crack patterns in the PVD coatings at  $345^\circ\text{C}$  compared with the RT tests: (i) the orientation of the coating cracks showed a larger deviation from the hoop direction ( $75^\circ$  to  $109^\circ$  at  $345^\circ\text{C}$ ), as shown in Fig. 13, and (ii) the width of these cracks were larger ( $1\text{--}8 \mu\text{m}$ ) after peak load (Fig. 13); (iii) the distance between coating cracks was also larger (Fig. 15b). The exact reason for these two types of behaviour is not fully understood, but this could be related to a similar thermal mismatch on heating, as observed in the cold sprayed coatings. This would result in change of stress-state, as well as a potential transition from brittle to ductile behaviour with increasing temperature which would lead to larger crack width and a reduced saturated crack density [16]. Indeed, further experiments with intermediate temperature steps should be conducted in the future to investigate the brittle to ductile transition temperature of such coating materials.

In general, the failure process of the PVD Cr-coated cladding materials tested at both RT and  $345^\circ\text{C}$  can be classified into three stages: (i) the initial collective deformation in the coating/substrate system without crack formation; (ii) multiple coating cracks formed simultaneously at  $\sim 80\%$  of peak load, with crack orientations diverged away from tensile hoop direction at higher temperature, and (iii) a much smaller distance between the coating cracks than the CS materials which steadily decreases to about 50–60% of the crack formation distance at peak load. It should be noted that with CS materials tested at RT, the distance between the coating cracks at peak load also decreased about by  $\sim 60\%$  compared to that at initial crack formation.

For both the CS and PVD materials, distance between coating cracks increased with increasing temperatures. Similar phenomenon has been reported, Jiang et al. [16] (2021) performed *in situ* tensile tests on their PVD Cr-coated (coating thickness:  $\sim 15 \mu\text{m}$ ) Zircaloy sheet specimens at elevated temperatures (from RT to  $300^\circ\text{C}$ ), and the distance between coating cracks were also reported to be increasing from  $\sim 66 \mu\text{m}$  at RT to  $\sim 166 \mu\text{m}$  at  $300^\circ\text{C}$  (in current work, it is  $\sim 30 \mu\text{m}$  at RT and  $\sim 50 \mu\text{m}$  at  $345^\circ\text{C}$  for PVD materials). Although different values were reported, which may be due to the variation of Cr coatings (coating thicknesses, fabrication processes) and testing configurations, similar trend was observed, again indicated the C-ring compression tests in current work is comparable with other test configurations, and indicated the quantitative analyses of the distance between coating cracks in current work is an effective method to investigate the coating crack behaviours.

## 5. Conclusions

The coating microstructure, local properties and the failure processes of two types of Cr coatings on nuclear Zircaloy cladding tube materials (cold sprayed (CS) and physical vapour deposited (PVD)) were investigated. The formation and propagation of coating cracks in a C-ring compression loading configuration were successfully imaged and studied at ambient and  $345^\circ\text{C}$  using real-time 3D synchrotron X-ray computed microtomography assisted by *ex situ* scanning electron microscope imaging.

The different manufacturing processes of CS and PVD methods resulted in different local microstructures and properties of the Cr coatings: for CS Cr-coated materials, high speed spraying process resulted in hardening in the substrate close to the interface; as for PVD

Cr-coated materials, smaller Cr grains close to interface caused higher hardness in the coating.

For both CS and PVD cladding materials, the measured hoop strengths at  $345^\circ\text{C}$  were  $\sim 50\%$  of the room temperature strengths; compared with PVD materials,  $\sim 14\%$  higher strength of first coating cracks' formation was found for CS materials tested at the same temperature, which can be potentially attributed to the higher interfacial roughness and splatted Cr grains in the CS Cr coatings.

For both types of materials tested at both temperatures, all the coating cracks arrested at the coating/substrate interface and did not penetrate the substrate; using first Dundurs parameter, based on measured local properties in current work and literature values on fracture toughness, the interfacial toughness of the CS material was estimated to be higher than the PVD materials at room temperature, and this was deemed to be plausible as the cold sprayed coating-substrate system had a more tortuous interlocking interface.

The failure processes of both types of coatings were investigated. CS coatings have a much larger overall distance between coating cracks at both RT and  $345^\circ\text{C}$  compared to the PVD coatings; in particular, the average distance between primary cracks for the CS coatings at  $345^\circ\text{C}$  was much larger than that at RT. The formation of tortuous fine cracks was found in the CS coatings only at  $345^\circ\text{C}$  during initial stage of loading. Once the primary cracks formed at  $345^\circ\text{C}$  due to the high tensile hoop stress, they did not increase in numbers but increased in width as the load was raised to peak load. For PVC coatings, the average distances between cracks at both RT and  $345^\circ\text{C}$  showed decreasing trend to 50–60% in the crack distance at peak load compared to the situation at their initial formation; in addition to the increase in the number of cracks, the PVD coatings at  $345^\circ\text{C}$  showed a widening of cracks with increasing load that demonstrated more ductile behaviour. The orientation of the cracks in the PVD coatings also showed larger deviation from the perpendicular direction of the tensile hoop stress. In both the CS and PVD coatings, the primary cracks (except those tortuous fine cracks in CS at  $345^\circ\text{C}$ ) were all formed simultaneously at about 80–90% of the peak load, a situation that did not change with temperature.

In summary, nuclear CS and PVD coatings demonstrate very different behaviour with testing temperature in a C-ring compression test configuration. The experimental observations in the current work are critical for faithful modelling of the mechanical behaviour and failure processes of these materials at elevated temperatures, and improving the design of these coated Zircaloy cladding materials for nuclear application. Future work with smaller temperature steps could offer better insights to the brittle to ductile transition temperature of the PVD coatings.

## Declaration of Competing Interest

The authors declare that they have no known competing financial interests or personal relationships that could have appeared to influence the work reported in this paper.

## Data availability

Data will be made available on request.

## Acknowledgements

D.L. acknowledges funding support from UK EPSRC (EP/T000368/1, EP/N004493/2). The authors also acknowledge the use of the X-ray synchrotron micro-tomography beamline (8.3.2) at the Lawrence Berkeley National Laboratory's Advanced Light Source, which is supported by the Office of Science of the U.S. Department of Energy under contract no. DE-AC02-05CH11231. Thanks are also due to Dr. Dula Parkinson for help with these synchrotron tomography experiments.

## Appendix A. Supplementary data

Supplementary data to this article can be found online at <https://doi.org/10.1016/j.matdes.2023.112373>.

## References

- [1] K.A. Terrani, Accident tolerant fuel cladding development: Promise, status, and challenges, *Journal of Nuclear Materials* 501 (2018) 13–30, <https://doi.org/10.1016/j.jnucmat.2017.12.043>.
- [2] H. Swan, M.S. Blackmur, J.M. Hyde, A. Laferrere, S.R. Ortner, P.D. Styman, C. Staines, M. Gass, H. Hulme, A. Cole-Baker, P. Frankel, The measurement of stress and phase fraction distributions in pre and post-transition zircaloy oxides using nano-beam synchrotron x-ray diffraction, *Journal of Nuclear Materials* 479 (2016) 559–575, <https://doi.org/10.1016/j.jnucmat.2016.07.024>.
- [3] R.V. Umretiya, B. Elward, D. Lee, M. Anderson, R.B. Rebak, J.V. Rojas, Mechanical and chemical properties of PVD and cold spray cr-coatings on Zircaloy-4, *Journal of Nuclear Materials* 541 (2020) 152–420, <https://doi.org/10.1016/j.jnucmat.2020.152420>.
- [4] A. Fazi, K. Stiller, H.O. Andrén, M. Thuvander, Cold sprayed cr-coating on optimized ZIRLO™ claddings: The Cr / Zr interface and its microstructural and chemical evolution after autoclave corrosion testing, *Journal of Nuclear Materials* 560 (2022) 153–505, <https://doi.org/10.1016/j.jnucmat.2022.153505>.
- [5] Y. Chen, J. Marrow, Effect of irradiation swelling on the mechanical properties of unidirectional SiC/SiC composites: A numerical investigation at microstructural level, *Journal of Nuclear Materials* 569 (2022) 153–918, <https://doi.org/10.1016/j.jnucmat.2022.153918>.
- [6] B. Maier, H. Yeom, G. Johnson, T. Dabney, J. Walters, P. Xu, J. Romero, H. Shah, K. Sridharan, Development of cold spray chromium coatings for improved accident tolerant zirconium-alloy cladding, *Journal of Nuclear Materials* 519 (2019) 247–254, <https://doi.org/10.1016/j.jnucmat.2019.03.039>.
- [7] K. Quillin, H. Yeom, T. Dabney, E. Willing, K. Sridharan, Microstructural and nanomechanical studies of PVD Cr coatings on SiC for LWR fuel cladding applications, *Surface and Coating Technology* 441 (2022), 128577, <https://doi.org/10.1016/j.surfcoat.2022.128577>.
- [8] T. Koyanagi, Y. Katoh, T. Nozawa, Design and strategy for next-generation silicon carbide composites for nuclear energy, *Journal of Nuclear Materials* 540 (2020) 152–375, <https://doi.org/10.1016/j.jnucmat.2020.152375>.
- [9] M. Ševceček, A. Gurgun, A. Seshadri, Y. Che, M. Wagih, B. Phillips, V. Champagne, K. Shirvan, Development of cr cold spray e coated fuel cladding with enhanced accident tolerance, *Nuclear Engineering and Technology* 50 (2) (2018) 229–236, <https://doi.org/10.1016/j.net.2017.12.011>.
- [10] U. Holzwarth, H. Stamm, Mechanical and thermomechanical properties of commercially pure chromium and chromium alloys, *Journal of Nuclear Materials* 300 (2–3) (2002) 161–177, [https://doi.org/10.1016/S0022-3115\(01\)00745-0](https://doi.org/10.1016/S0022-3115(01)00745-0).
- [11] A. Fazi, H. Aboulfadl, A.H. Iyer, M. Sattari, K.M. Stiller, P. Lokhande, M. Thuvander, H.O. Andrén, Characterization of as-deposited cold sprayed cr-coating on optimized ZIRLO™ claddings, *Journal of Nuclear Materials* 549 (2021) 152–892, <https://doi.org/10.1016/j.jnucmat.2021.152892>.
- [12] S. Shahidi, B. Moazzenchi, M. Ghoranneviss, A review-application of physical vapor deposition (PVD) and related methods in the textile industry, *European Physical Journal Applied Physics* 71 (3) (2015) 31302, <https://doi.org/10.1051/epjap/2015140439>.
- [13] D.C. Roache, C.H. Bumgardner, T.M. Harrell, M.C. Price, A. Jarama, F.M. Heim, J. Walters, B. Maier, X. Li, Unveiling damage mechanisms of chromium-coated zirconium-based fuel claddings at LWR operating temperature by in-situ digital image correlation, *Surface and Coating Technology* 429 (2022), 127909, <https://doi.org/10.1016/j.surfcoat.2021.127909>.
- [14] Burden DE, Harrell TM, Bumgardner CH, Roache DC, Walters JL, Lahoda E, Maier BR, Li X, Unveiling Fracture Mechanics of a Curved Coating/Substrate System by Combined Digital Image Correlation and Numerical Finite Element Analyses, under pear review, [https://papers.ssrn.com/sol3/papers.cfm?abstract\\_id=4419793](https://papers.ssrn.com/sol3/papers.cfm?abstract_id=4419793).
- [15] D.V. Nguyen, M. Le Saux, L. Gélébart, J.C. Brachet, J.P. Bonthonneau, A. Courcelle, R. Guillou, E. Rouesne, S. Urvoy, Mechanical behavior of a chromium coating on a zirconium alloy substrate at room temperature, *Journal of Nuclear Materials* 558 (2022) 153–332, <https://doi.org/10.1016/j.jnucmat.2021.153332>.
- [16] J. Jiang, H. Zhai, M. Du, D. Wang, X. Pei, X. Ma, B. Wang, Temperature-dependent deformation and cracking behavior in Cr coating for accident tolerant fuel cladding: An in situ SEM study, *Surface and Coating Technology* 427 (2021), 127815, <https://doi.org/10.1016/j.surfcoat.2021.127815>.
- [17] B. Bandi, S.K. Dinda, J. Kar, G.G. Roy, P. Srirangam, Effect of weld parameters on porosity formation in electron beam welded Zircaloy-4 joints: X-ray tomography study, *Vacuum* 158 (2021) 172–179, <https://doi.org/10.1016/j.vacuum.2018.09.060>.
- [18] L. Saucedo-Mora, T. Lowe, S. Zhao, P.D. Lee, P.M. Mummery, T.J. Marrow, In situ observation of mechanical damage within a SiC-SiC ceramic matrix composite, *Journal of Nuclear Materials* 481 (2016) 13–23, <https://doi.org/10.1016/j.jnucmat.2016.09.007>.
- [19] J.P. Forna-Kreutzer, J. Ell, H. Barnard, T.J. Pirzada, R.O. Ritchie, D. Liu, Full-field characterisation of oxide-oxide ceramic-matrix composites using x-ray computed micro-tomography and digital volume correlation under load at high temperatures, *Materials and Design* 208 (2021), 109899, <https://doi.org/10.1016/j.matdes.2021.109899>.
- [20] G. Yuan, J.P. Forna-Kreutzer, P. Xu, S. Gonderman, C. Deck, L. Olson, E. Lahoda, R. O. Ritchie, D. Liu, in situ high-temperature 3D imaging of the damage evolution in a SiC nuclear fuel cladding material, *Materials and Design* 227 (2023), 111784, <https://doi.org/10.1016/j.matdes.2023.111784>.
- [21] T.J. Pirzada, D. Liu, J. Ell, H. Barnard, I. Šulák, M. Galano, T.J. Marrow, R. O. Ritchie, In situ observation of the deformation and fracture of an alumina-alumina ceramic-matrix composite at elevated temperature using x-ray computed tomography, *Journal of the European Ceramic Society* 41 (7) (2021) 4217–4230, <https://doi.org/10.1016/j.jeurceramsoc.2021.01.030>.
- [22] A.S.T.M. Standard C1323–26, Standard Test Method for Ultimate Strength of Advanced Ceramics with Diametrically Compressed C-Ring Specimens at Ambient Temperature 2016 ASTM International West Conshohocken, PA 10.1520/C1323-16.2.
- [23] J. Kim, S. Joong, Y. Lee, Effect of cr coating on the mechanical integrity of accident tolerant fuel cladding under ring compression test, *Journal of Nuclear Materials* 585 (2023) 154–603, <https://doi.org/10.1016/j.jnucmat.2023.154603>.
- [24] G.F. Vander Voort, Metallographic specimen preparation for electron backscatter diffraction part II, *Pract. Metallogr.* 48 (10) (2011) 527–543.
- [25] T. Ajantivayal, T. Trowbridge, A. Winston, C. Sun, K. Sridharan, A. Aitkaliyeva, X. best practices for preparing radioactive specimens for EBSD analysis, *Micron* 118 (2019) 1–8.
- [26] W.C. Oliver, G.M. Pharr, An improved technique for determining hardness and elastic modulus using load and displacement sensing indentation experiments, *Journal of Materials Research* 7 (6) (2012) 1564–1583, <https://doi.org/10.1557/JMR.1992.1564>.
- [27] S. Suman, M.K. Khan, M. Pathak, R.N. Singh, investigation of elevated-temperature mechanical properties of  $\delta$ -hydride precipitate in Zircaloy-4 fuel cladding tubes using nanoindentation, *Journal of Alloys and Compounds* 726 (2017) 107–113, <https://doi.org/10.1016/j.jallcom.2017.07.321>.
- [28] D. Liu, B. Gludovatz, H.S. Barnard, M. Kuball, R.O. Ritchie, Damage tolerance of nuclear graphite at elevated temperatures, *Nature Communications* 8 (1) (2017) 15942, <https://doi.org/10.1038/ncomms15942>.
- [29] H.A. Bale, A. Haboub, A.A. MacDowell, J.R. Nasiatka, D.Y. Parkinson, B.N. Cox, D. B. Marshall, R.O. Ritchie, Real-time quantitative imaging of failure events in materials under load at temperatures above 1600°C, *Nature Materials* 12 (1) (2013) 40–46, <https://doi.org/10.1038/nmat3497>.
- [30] H. Barnard, D.Y. Parkinson, B. Gludovatz, A. Haboub, N. Larson, F. Zok, F. Panerai, N.N. Mansour, H. Bale, C. Acevedo, D. Liu, High temperature x-ray micro-tomography, *American Institute of Physics Conference Proceedings* 1417 (1) (2016) 5–9, <https://doi.org/10.1063/1.4952925>.
- [31] T.L. Embree, A.E. Segall, Evaluation of the uniaxiality of the stress state in c-ring fracture strength specimens, *Journal of Testing and Evaluation* 32 (2) (2004) 153–160, <https://doi.org/10.1520/jte11965>.
- [32] M.A. Yakovlev, D.J. Vanselow, M.S. Ngu, C.R. Zaino, S.R. Katz, Y. Ding, D. Parkinson, S.Y. Wang, K.C. Ang, P. La Riviere, K.C. Cheng, A wide-field micro-computed tomography detector: micron resolution at half-centimetre scale, *Journal of Synchrotron Radiation* 29 (2) (2022) 505–514, <https://doi.org/10.1107/S160057752101287X>.
- [33] D. Gürsoy, F. De Carlo, X. Xiao, C. Jacobsen, TomoPy: a framework for the analysis of synchrotron tomographic data, *Journal of Synchrotron Radiation* 21 (5) (2014) 1188–1193, <https://doi.org/10.1107/S1600577514013939>.
- [34] T. Ferreira, W. Rasband, *ImageJ User Guide IJ 1* (2012) 46r.
- [35] *User's Guide* (2018).
- [36] T.C. Reiley, W.D. Nix, The structure and mechanical properties of physically vapor deposited chromium, *Metall Mater Trans A Phys Metall Mater Sci METALL MATER TRANS A* (1976) 1695–1701, <https://doi.org/10.1007/BF02817887>.
- [37] T. Graening, C.P. Massey, K. Linton, A. Nelson, *Microstructure investigation and mechanical properties of coated zircaloy cladding*, No. (ORNL/SPR-2021/203.).
- [38] Calla E, McCartney DG, Shipway PH, Effect of deposition conditions on the properties and annealing behavior of cold-sprayed copper. *J. Therm. Spray Technol.* 15 (2006) 255–262, <https://doi.org/10.1361/105996306X108192>.
- [39] Y. Zou, W. Qin, E. Irrissou, J.G. Legoux, S. Yue, J.A. Szpunar, Dynamic recrystallization in the particle/particle interface region of cold-sprayed nickel coating: Electron backscatter diffraction characterization, *Scripta Materialia* 61 (9) (2009) 899–902, <https://doi.org/10.1016/j.scriptamat.2009.07.020>.
- [40] J.C. Brachet, I. Idarraga-Trujillo, M. Le Fleu, M. Le Saux, V. Vandenberghe, S. Urvoy, E. Rouesne, T. Guilbert, C. Toffolon-Masclat, M. Tupin, C. Chalippou, Early studies on Cr-Coated Zircaloy-4 as enhanced accident tolerant nuclear fuel claddings for light water reactors, *Journal of Nuclear Materials* 517 (2019) 268–285, <https://doi.org/10.1016/j.jnucmat.2019.02.018>.
- [41] D.C. Roache, A. Jarama, C.H. Bumgardner, F.M. Heim, J. Walters, J. Romero, B. Maier, X. Li, Unveiling damage mechanisms of chromium-coated zirconium-based fuel claddings by coupling digital image correlation and acoustic emission, *Materials Science and Engineering A* 774 (2020), 138850, <https://doi.org/10.1016/j.msea.2019.138850>.
- [42] H. Ming-Yuan, J.W. Hutchinson, Crack deflection at an interface between dissimilar elastic materials, *International Journal of Solids and Structures* 25 (9) (1989) 1053–1067, [https://doi.org/10.1016/0020-7683\(89\)90021-8](https://doi.org/10.1016/0020-7683(89)90021-8).
- [43] D. Liu, S. Fabes, B.S. Li, D. Francis, R.O. Ritchie, M. Kuball, Characterization of the interfacial toughness in a novel “GaN-on-diamond” material for high-power RF devices, *ACS Appl. Electron. Mater.* 1 (3) (2019) 354–369, <https://doi.org/10.1021/acsaem.8b00091>.
- [44] Ren Y. Fracture toughness behavior of Zircaloy-4 in the form of fuel cladding tubing in nuclear reactors. 2004.
- [45] D.W. Green, M.Z. Southard, *Perry's chemical engineers' handbook*. McGraw-Hill, Education (2019).

- [46] W.M. Haynes, *CRC handbook of chemistry and physics*, CRC Press, 2016.
- [47] A.H. de Menibus, T. Guilbert, Q. Auzoux, C. Toffolon, J.C. Brachet, J.L. Bechade, Hydrogen contribution to the thermal expansion of hydrided Zircaloy-4 cladding tubes, *Journal of Nuclear Materials* 440 (1–3) (2021) 169–177, <https://doi.org/10.1016/j.jnucmat.2013.04.039>.
- [48] O. Zanellato, M. Preuss, J.Y. Buffiere, F. Ribeiro, A. Steuwer, J. Desquines, J. Andrieux, B. Krebs, Synchrotron diffraction study of dissolution and precipitation kinetics of hydrides in Zircaloy-4, *Journal of Nuclear Materials* 420 (1–3) (2012) 537–547, <https://doi.org/10.1016/j.jnucmat.2011.11.009>.